Series Interconnects and Charge Extraction Interfaces for Hybrid Solar Cells

Andrew Stuart Hey

Brasenose College

Thesis submitted for the degree of Doctor of Philosophy

University of Oxford

April 2013

For my Parents and for Ruth

Declaration

Except where explicitly stated, the material contained in this thesis is wholly the result of my own work and was not produced as part of any collaboration. No part of this thesis has been submitted for any other qualification in this University or elsewhere.

Andrew Hey

April 2013

Abstract

This thesis investigates novel hole extraction interfaces and series interconnects for applications in organic photovoltaics, specifically in single junction solid-state dye-sensitized solar cells (DSSCs) and tandem DSSC/polymer bulk heterojunction solar cells. Improvements in hole extraction and device performance by using materials compatible with scalable deposition methods are presented, including tungsten- and molybdenum-disulphide (WS_2 and MoS_2), and *p*-type doped spiro-OMeTAD (2,2',7,7'-tetrakis-(N,N-di-p-methoxyphenylamine)9,9'-spirobifluorene) nanoparticle dispersions. WS_2 and MoS_2 hole extraction layers increase averaged short circuit currents by 20% and 16% respectively, and power conversion efficiencies by 19% and 14% respectively when compared with control devices. Similarly, doped spiro-OMeTAD nano-particle layers improved short circuit current densities by 32% and efficiencies by 9%. Tandem device interconnects using these novel hole extraction formats have been fabricated, but although devices did exhibit rectification, overall performance was poor. Possible reasons for their limited success have been analysed.

Dye-sensitized solar mini-modules are also reported. In order to assure the scalability of DSSC technology, these larger area devices were constructed

using doctor blade coating to deposit the hole transporter material. As well as achieving a respectable maximum power conversion efficiency of 2.6%, it has also been shown that the extent to which hole transporter infiltrates the mesoporous photoanode of these devices may be tuned by altering substrate temperature during deposition. It was found that an optimal coating temperature of 70°C produced the best efficiency, with a corresponding pore-filling fraction of 41%.

Acknowledgments

I offer my gratitude firstly to Dr Henry Snaith for his guidance, support, and for providing the opportunity to engage in this research. Without his constant flow of ideas and indefatigable optimism in the face of all setbacks, this project would simply not have been possible. I also acknowledge the Engineering and Physical Sciences Research Council for providing the funding to undertake this work, as part of the SUPERGEN project. Thanks also to Prof Valeria Nicolosi, whose materials have been utilised in parts of this thesis, and to Dr Pablo Docampo for valuable discussion related to pore-filling measurements.

I would like to thank all members of the Oxford Photovoltaic and Optoelectronic Device Group both present and past for always being willing to help and to teach without hesitation, and for doing so with infinite patience. I am grateful for the good friends made and the time spent among such talented and affable colleagues.

Finally special thanks to my Parents and my partner Ruth, whose unwavering confidence, support and encouragement have helped me beyond measure throughout the last four years and to whom I am greatly indebted.

Contents

Abstract **ii**

Acknowledgments **iv**

List of Figures **viii**

1 Introduction **1**

1.1 Inorganic Photovoltaics 3

1.2 Organic and Hybrid Photovoltaics 5

1.2.1 Dye-Sensitized Solar Cells 6

1.2.2 Tandem and Multiple Junction Solar Cells 13

1.2.3 Bulk Heterojunction Solar Cells 15

2 Experimental methods **20**

2.1 Standard Device Fabrication 20

2.1.1 DSSC fabrication 20

2.1.2 BHJ solar cell fabrication 23

2.1.3 Mesoporous aluminium oxide synthesis 24

2.2 Device and Material Characterisation 25

2.2.1 Current-Voltage Measurements 25
2.2.2 Contact resistance and conductivity measurements 29
2.2.3 Pore-filling measurement 31
2.2.4 Scanning electron microscopy 34

3 Transition metal dichalcogenide (TMDC) charge extraction interfaces 35
3.1 Experimental details 40
3.2 Results and discussion 41
3.2.1 TMDC film characterisation 41
3.2.2 Device performance 45
3.3 Conclusion 53

4 Doped organic semiconductor nanoparticle dispersions 54
4.1 Experimental details 57
4.1.1 Synthesis 57
4.1.2 Device fabrication 58
4.2 Results and discussion 59
4.3 Conclusion 70

5 Tandem devices 71
5.1 Sub-cells 71
5.2 Recombination interfaces 73
5.3 Experimental details 77
5.4 Results and discussion 79

5.5 Conclusion 89

6 Large area hole transporter deposition in mini-modules 90

6.1 Experimental details 94

6.2 Results and discussion 95

6.3 Conclusion 101

7 Conclusions 102

7.1 Potential future work 104

Appendix 107

Publications 107

International conference poster presentations 108

List of Figures

1.1 Inorganic photovoltaic operation 5

1.2 Illustrative energy level diagram for a solid-state DSSC 9

1.3 Solid-state DSSC structure 10

1.4 Chemical structure of spiro-OMeTAD 11

1.5 Spectrum of solar radiation at the earths surface 15

1.6 BHJ solar cell operation and structure 17

2.1 DSSC electrode schematic 21

2.2 An example current density-voltage curve 26

2.3 Equivalent circuit for a solar cell 27

2.4 The effect of parasitic resistances on current density-voltage characteristics 28

2.5 Four terminal electrode pattern for measurement of contact resistance 29

2.6 Equivalent circuit for contact resistance measurement 30

3.1 Spiro-OMeTAD/TMDC junction band diagram 39

3.2 Different band bending scenarios at a spiro-OMeTAD/TMDC junction 39

3.3 Absorbance spectra of films of WS_2 and MoS_2 42
3.4 SEM images of WS_2 film deposited by spray pyrolysis 43
3.5 SEM images of MoS_2 film deposited by spray pyrolysis 44
3.6 Performance of DSSCs with TMDC interfacial layers 46
3.7 Averaged current-voltage curves for DSSCs with TMDC interfacial layers 47
3.8 Example current density-voltage curves for DSSCs using PEDOT:PSS, WS_2 and MoS_2 hole extraction layers 47
3.9 Cross sectional structure of TMDC contact resistance samples 49
3.10 Sample and contact resistances for WS_2 and MoS_2 on spiro-OMeTAD 51
3.11 Device performance with changing thickness of MoS_2 52
3.12 Current density-voltage curves as a function of different numbers of MoS_2 coats 52

4.1 Spiro-OMeTAD/p-type spiro-OMeTAD junction band diagram 55
4.2 Nanoparticle dispersion synthesis 56
4.3 Performance of DSSCs with p-type spiro-OMeTAD and n-type PCBM nanoparticle interfacial layers 61
4.4 Averaged current density-voltage plots for DSSCs with and without p-spiro-OMeTAD interfacial layer 62
4.5 Averaged current density-voltage characteristics of doped nanoparticle diodes 63
4.6 Performance of D102-sensitized DSSCs with p-spiro-OMeTAD/n-PCBM diode coated on top 64

4.7 Spiro-OMeTAD nanoparticle absorption spectrum 65
4.8 PCBM nanoparticle dispersion absorption spectra 65
4.9 Current density-voltage characteristics for P3HT:PCBM BHJ solar cells with PCBM nanoparticle interfacial layer 67
4.10 SEM images of doped spiro-OMeTAD nanoparticle film deposited by spin coating 68
4.11 SEM images of doped PCBM nanoparticle film deposited by spin coating 69

5.1 DSSC and BHJ absorption spectra comparison 73
5.2 Illustrative energy bands for a generic tandem DSSC 74
5.3 Summary of TMDC and doped nanoparticle absorbance characteristics 76
5.4 Tandem cell cross section schematic 79
5.5 Averaged current density-voltage curves for tandem cells using PEDOT:PSS/TiO_2 interconnect and for sub-cells 80
5.6 Averaged current density-voltage curves for tandem cells using PEDOT:PSS/TiO_2 and doped spiro-OMeTAD nanoparticle/ TiO_2 interconnects 81
5.7 Open-circuit voltages of tandem solar cells employing PEDOT:PSS/ TiO_2 and doped spiro-OMeTAD nanoparticle/TiO_2 interconnects, and of their sub-cells 82
5.8 Modelling ideal tandem cell performance using sub-cell characteristics 84

5.9 Simulated current density-voltage curve for tandem devices with perfect interconnects 85

5.10 SEM image of spiro-OMeTAD surface of DSSC sub-cell with and without PEDOT:PSS 87

5.11 SEM images of TiO_2 nanoparticle film deposited by spin casting on top of PEDOT:PSS-coated DSSC sub-cell 88

6.1 a) Schematic showing the cross section of a mini-module. b) Diagram illustrating the process of doctor-blading 93

6.2 Large area mini-module performance parameters 99

6.3 Example transmission spectra for a sample of TiO_2 showing Fresnel interference fringes and hole transporter pore-filling fraction as a function of temperature 100

Chapter 1

Introduction

Ever more urgency is being placed on finding viable methods to utilise renewable energy sources. Concern over the threat of climate change induced by greenhouse gasses released during the combustion of fossil fuels is ongoing, and resources of coal, oil and natural gas are expected to become increasingly scarce. The future of nuclear power generation is also far from certain.Continued public unease has been bolstered by the disastrous events of 2011 at the Fukushima Daiichi reactors in Japan, with Germany already committed to phasing out its nuclear infrastructure. [1] These issues are set against a backdrop of increasing demand for energy, with recent predictions suggesting that global annual energy consumption could exceed 800EJ by 2050. [2]

Solar energy represents a huge potential resource: estimates as to its actual realisable annual energy potential vary from 118EJ to 2592EJ (taking factors such as available land with appropriate illumination, and environmental and social considerations into account), but as of the end of 2011

there was only 65GW (equivalent to about 2EJ annually) of installed photovoltaics (PV) — a tiny fraction of current global energy demand (514EJ were consumed in 2008). [2, 3] Traditional inorganic photovoltaic technology can attain high power conversion efficiency, though fabrication is energy intensive and requires high temperature and vacuum processing techniques. The high cost associated with manufacture makes the technology uneconomical and it is for this reason that it has had little uptake — the U.S. Energy Information Administration has forecast electricity generated by PV installations brought online in 2017 would cost 152.7$/MWh compared to 66.1$/MWh for gas. [4]

Using solution processable organic and inorganic semiconducting materials to make photovoltaic devices presents an appealing alternative route for harvesting solar energy. Not only do they offer potentially cheaper and less energy intensive reel to reel manufacturing techniques that are already well established in other industries, but the vast range of materials and combinations available give the opportunity for fine tuning of optical and electronic properties. Additionally many systems in this broad field can be made semi-transparent. This opens up opportunities for their integration into buildings as windows, increasing the surface area available on which to employ photovoltaics in an urban context. Once these technologies reach power conversion efficiencies comparable to those of traditional inorganic PV, it is hoped a significantly lower cost per kWh will encourage widespread uptake of solar electricity generation.

It is within this context that this thesis is presented. A number of modifications to improve the performance of current state-of-the-art organic and hybrid photovoltaics are presented, as well as investigation into the scalabil-

ity of such devices. It is hoped that these steps may contribute to achieving an efficient, cheap and commercially viable technology that will encourage meaningful exploitation of the solar resource.

1.1 Inorganic Photovoltaics

Much research into inorganic semiconductor solar cells has been undertaken since their inception. The first silicon p-n junction device reported by Chapin et al. in 1954 offered 6% power conversion efficiency — today's crystalline silicon photovoltaics have achieved verified efficiencies of 25%, and those based on GaAs almost 30%. [5,6] When photons with an energy greater than that of the band gap of the semiconductor are incident on these kinds of device, they can be absorbed, promoting an electron from the valance to the conduction band and leaving a positively charged hole in its place. To make use of this phenomenon to generate electricity, the excited charges must be removed from the device. Doping such semiconductors with impurity atoms can add to the number of electrons (n-type) or holes (p-type) present in the conduction band or valance band respectively at the operating temperatures of a solar cell. This shifts the position of the Fermi levels to higher or lower energies within the band gap relative to the intrinsic semiconductor — when n-type and p-type doped semiconductor are brought into intimate contact the Fermi levels either side of the junction must align. The result is that the absolute position of the valance and conduction bands is different on either side of the junction. [7] When integrated into a device the steps in band potential act both as one-way barriers for electrons and holes and as

a source of in-built electric field — electrons may only drift from the p- to the n-type region and holes from n- to p-type (figure 1.1a). This separates charge carrier species spatially, which can then be extracted through the use of suitable electrodes. Though this system has been made to work very well, a fundamental flaw is that both species of charge carriers are present in both n- and p-type regions since light of suitable wavelengths can be absorbed at any point spatially, regardless of doping. This requires that the semiconductor must have extremely low levels of impurities — impurities commonly add available electronic states within the band gap at their location, and act as recombination sites for nearby electrons and holes as shown in figure 1.1b. [8] It is this that necessitates the high levels of deposition control afforded by the high temperature vacuum processing techniques used, and ultimately makes them economically unattractive for large scale electricity production.

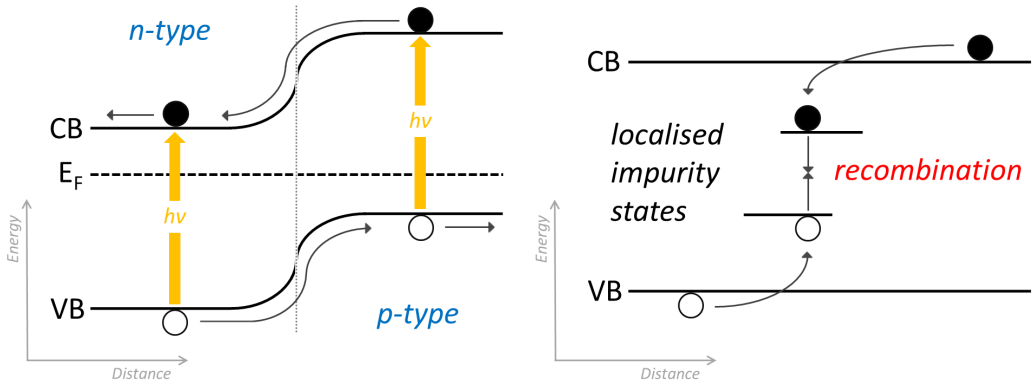

(a) (b)

Figure 1.1: Inorganic photovoltaic operation. 1.1a) Demonstration of charge generation and separation as described in the text. 1.1b) The effect of impurity inclusion in inorganic solar cells — charge carriers in either band of the bulk semiconductor material may become trapped in localised sub-band gap states due to the impurity material making recombination with carriers of opposite charge in their bulk energy band (or in nearby trap sites) more likely.

1.2 Organic and Hybrid Photovoltaics

Research into use of organic semiconductor materials to generate photovoltage began in the 1950s, though the broad range of present technologies encompassed by the field of organic and hybrid photovoltaics has not yet matched the achievements of inorganic PV. [6, 9] Solar cells in this classification typically use organic molecules or polymers as the photoactive component. One of their great attractions is the vast array of materials with suitable properties both optically and electronically, and the option to chemically design and synthesize new ones with desirable characteristics. This allows solar cells to be finely tuned, for example they may be made active over different sections of the solar spectrum through choice of absorber.

Organic semiconductors typically have much lower dielectric constants

than their inorganic counterparts, and as such the electron and hole created on absorption of above band gap radiation have a strong coulomb interaction that results in them existing in a tightly bound state, or exciton, that will not dissociate thermally at room temperature (binding energy $\propto \epsilon_r^{-1}$). This is different to the case of inorganic semiconductors where the dielectric constant is higher (for silicon $\epsilon_r = 11.7$ [10]) and charges will dissociate relatively easily. This leads to organic and hybrid photovoltaics often being termed "excitonic" solar cells, and they require the use of a different mechanism for charge separation.

Of these organic technologies, one of the fore-runners in terms of power conversion efficiency is the dye-sensitized solar cell. It employs an elegant solution to the problem of charge separation and is compatible with many different organic absorber materials, thus its active spectral region can be easily modified. This system will be the primary focus of this thesis.

1.2.1 Dye-Sensitized Solar Cells

The generation of photovoltage through excitation of an inorganic absorber material was first demonstrated over a century ago by Moser, and has since been the focus of much research. [11] A breakthrough in the field came in the form of the dye-sensitized solar cell (DSSC), invented in 1991 by O'Regan and Grätzel. [12,13] These hybrid excitonic devices employ molecular organic dyes to generate excitons, and use the interface with a transition metal oxide to separate the charge carriers. Solar radiation of energy higher than the dye band gap will promote electrons from the highest occupied molecular

orbital of the dye (or HOMO, analogous to the valance band of inorganic semiconductors) to the lowest unoccupied molecular orbital (LUMO, analogous to a conduction band). The excited electron is then injected into to the metal oxide conduction band — critically the process of injection takes place on a timescale orders of magnitude faster than the relaxation time of the dye (femtoseconds to tens of nanoseconds, as opposed to microseconds), meaning charge separation dominates over recombination on the dye molecule. [14, 15] A medium is provided to regenerate the dye molecule now missing an electron, and appropriate electrodes complete the device. The most common metal oxide component in such cells, and the one used in the DSSC experiments presented herein, is TiO_2, though SnO_2 and ZnO may also be used. [16, 17] For effective charge separation to occur, any dye molecules must be in direct contact with the TiO_2 (or similar). Sensitization of the oxide should ideally only leave a monolayer of dye adsorbed on the surface for effective charge transfer. Since such a monolayer of organic dye molecules has only a small absorption cross-section, the vast majority of the solar radiation incident upon it will be transmitted straight through it. The solution to generating enough charge for efficient solar cell operation is to structure the oxide to increase the surface area of the interface with the dye. This structure can take a variety of forms (for example nanowire or nanotube arrays, or structures derived from block-copolymers [18–20]) but one of the most common is the mesoporous, sponge-like structure formed by sintering together TiO_2 nanoparticles around 20nm in diameter creating films with roughly 60% porosity, and is the type used in the experiments to follow. [14] Structures like this can be made several microns thick, enough to allow many

dyes to completely absorb all solar photons with wavelengths to which they are sensitive.

Electrons are thought to travel through the TiO_2 nanostructure to the anode via a process of trap-limited diffusion. Electron mobility is much slower in the nanostructure than in single crystals of TiO_2, and experiment and theory suggest this may be due to the existence of spatially localised trap states of lower energy than the conduction band. [14, 21, 22] Injected electrons will preferentially fill these trap states, and a thermal activation energy is required to promote them to the conduction band in which they are free to diffuse through the nanostructure before meeting another trap site or the anode.

To allow photons to enter the device, at least one of the electrodes must have high transmittance over the solar spectral range. Commonly either indium tin oxide (ITO) or fluorine-doped tin oxide (FTO, F:SnO_2) is used (both of which are adequately transparent and conductive), coated onto the glass substrate on which DSSC devices are fabricated. These oxides can accept electrons from TiO_2 and carry them to an external circuit. In DSSCs, the combination of transparent anode and mesoporous metal oxide is known as the photoanode.

To complete the device, the highest efficiency DSSCs use a liquid electrolyte containing a redox couple, such as the iodide/triiodide (I^-/I_3^-) system. The reduced iodide species donates an electron to regenerate a dye molecule leaving the resulting oxidized triiodide component to diffuse to the cathode, where it takes an electron from the external circuit via a platinum catalyst (this diffusion and reduction at the cathode is much faster than recombination

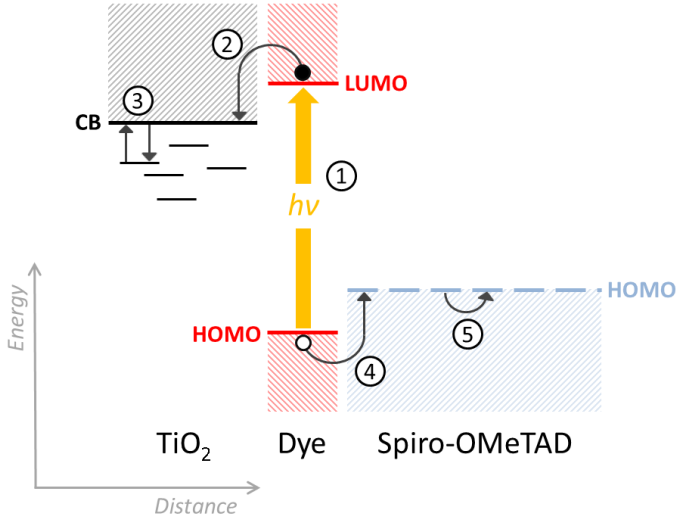

Figure 1.2: Illustrative energy level diagram for a solid-state DSSC outlining key processes for charge generation and transport as discussed in the text: 1. dye excitation by above-band gap radiation; 2. electron injection into TiO_2 conduction band; 3. electron transport limited by trapping and de-trapping in TiO_2 sub-band gap states; 4. hole injection into spiro-OMeTAD; 5. hole transport via hopping mechanism.

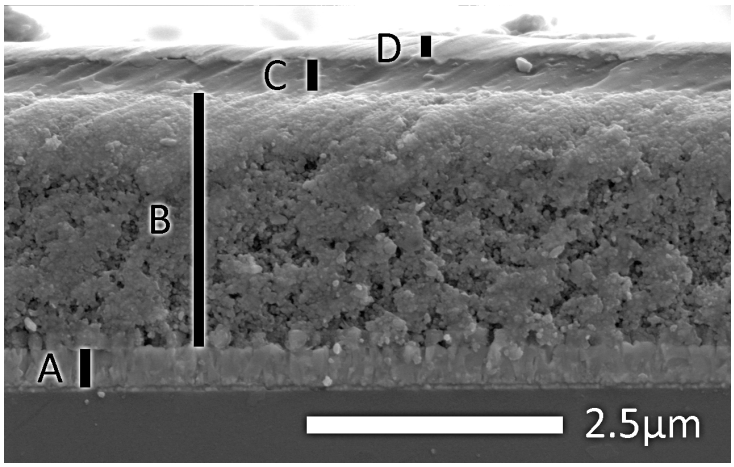

(a)

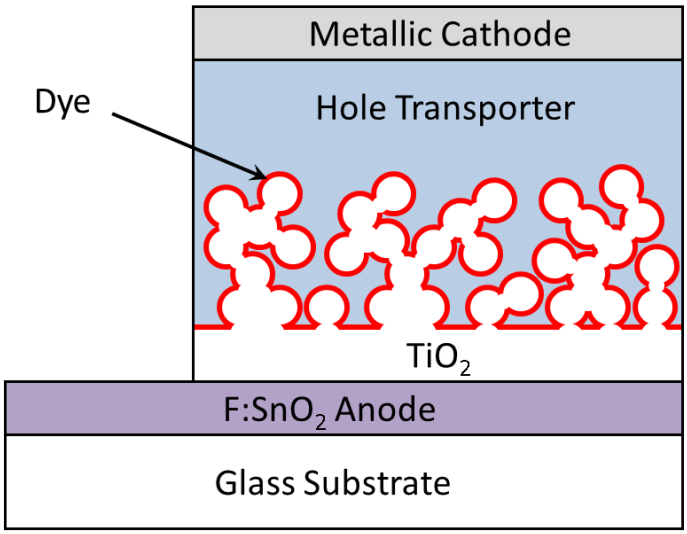

(b)

Figure 1.3: Solid-state DSSC structure. 1.3a) A cross-sectional SEM image of a typical device indicating regions of fluorine-doped tin oxide (A), TiO_2/dye/hole transporter (B), hole transporter capping layer (C) and silver cathode (D) — the region below layer A is glass. 1.3b) A simplified schematic illustrating the components seen in the SEM image.

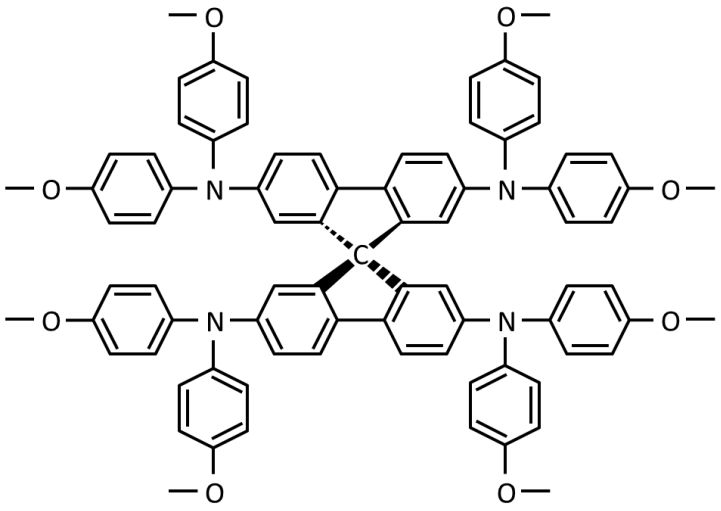

Figure 1.4: Chemical structure of the organic molecular hole transporter spiro-OMeTAD.

with the excess of electrons in the TiO_2 mesostructure, and allows effective solar cell operation). [23, 24] Unfortunately these electrolytes are often corrosive and utilise volatile solvents — sealing them within a completed device for long term practical use is difficult, and can have detrimental effects on the lifetime of the system. [25] Because complete electrode assembly is required before infiltrating the sealed device with the electrolyte, the practicalities of scaling devices to large areas are more challenging than for cells that may simply be processed layer upon layer. The inclusion of platinum is also not ideal considering its rarity and the long term goal to keep manufacturing costs as low as possible.

An alternative is to use a solid-state molecular hole transporter material (HTM), such as 2,2',7,7'-tetrakis-(N,N-di-p-methoxyphenylamine)9,9'-spirobifluorene (spiro-OMeTAD, figure 1.4) — an organic semiconductor with a band structure such that holes left on the excited dye molecules are trans-

ferred to its HOMO. [26] They may be cast from solution onto sensitized photoanodes, infiltrating the pores before the solvent evaporates leaving solid material. In conductive organic molecules such as spiro-OMeTAD strong charge carrier-phonon interactions lead to a "lattice distortion" — in order for charge to move, the distortion must also move. This coupling of charge and lattice distortion is termed a polaron, and requires that a characteristic activation energy be overcome for holes to move between molecules — this transport process is known as hole hopping and is somewhat analogous to electron transport in TiO_2. [14, 27] Deposition of an appropriate cathode completes the solid-state DSSC. The use of solid HTMs clearly does not pose the same associated stability and environmental concerns that surround the sealing of electrolytes, and as they can be incorporated into devices before the cathode is in place they lend themselves well to monolithic layer by layer fabrication — potentially ideal for scaling to large areas. Figure 1.2 shows the key charge generation and transport processes for a solid-state DSSC. The device architecture of a solid-state dye-sensitized solar cell is shown in figure 1.3.

Although the efficiencies of liquid electrolyte DSSCs are only now becoming competitive with commercial inorganic photovoltaics (the best verified efficiency being 11.9%), and solid-state DSSCs are still some way off (7.2% has been reported), this new technology presents significant potential advantages over traditional silicon-based PV with respect to fabrication on both fundamental and practical levels. [6, 28] The difference that has the largest impact on fabrication techniques and therefore cost is the fact that charge generation and separation occurs at a single interface in DSSCs, so unlike

inorganic *p*-*n* junctions, there are no minority carriers in the regions where majority carriers are being transported. Thus they are not as sensitive to impurities and do not require the intensive processing of inorganic PV. Any additional localised sub-band gap states in either the TiO_2 or spiro-OMeTAD caused by impurities may become charge carrier traps, but are unlikely to act as recombination centres.

The emphasis now is to enhance the performance of solid-state DSSCs to make them competitive with liquid-electrolyte DSSCs, and with traditional inorganic photovoltaics.

1.2.2 Tandem and Multiple Junction Solar Cells

The use of multiple junctions in DSSC devices presents one option for improving their performance. A dye molecule can typically absorb photons with a range of energies above that of its band gap. However much of the energy of the absorbed photons is lost as excited electrons relax thermally to the LUMO of the dye. A solution is to use an architecture employing multiple absorbers with different band gaps — larger band gap absorbers can harvest more energy from high energy photons whilst lower band gaps ensure that a high number of photons are being absorbed over a large range of the solar spectrum. Figure 1.5 shows the spectrum of solar radiation that reaches the surface of the Earth. [29]

A common multiple junction architecture for a range of photovoltaic technologies is to process several sub-cells on top of one another with series interconnects (or recombination layers) in between. [30] In such a system

conservation of charge dictates that the current produced by each sub-cell must be the same — if charge generation is greater in one sub-cell than the other, space charge will accumulate in regions within the device such that this condition is met. Assuming perfect interconnects the open circuit voltages of the sub-cells will add together. The ideal interconnect must make an ohmic contact to each adjoining sub-cell, be non-absorbing to allow the maximum number of photons to reach the next active layer, and have an appropriate energy level profile to allow electrons from one sub-cell to recombine efficiently with holes from the next. The discussion here will be limited to tandem (i.e. two sub-cell) hybrid devices. When fabricating the mesoporous TiO_2 photoanode it is necessary to heat substrates to 500°C (as will be discussed in section 2.1). The organic DSSC components, namely the dye and HTM, cannot withstand these temperatures, thus it is not currently possible to process solid-state DSSCs on top of each other as required for a tandem device. Instead a different system must be used as a "top" sub-cell, one that may be processed on top of a complete solid-state DSSC. A number of options are available, including organic bulk heterojunction (BHJ) solar cells. Bruder et al. reported the first entirely solid-state tandem DSSC device, using a zinc phthalocyanine:C_{60} BHJ cell deposited via thermal evaporation as the second active layer. [31] In the following discussion solution processable bulk heterojunctions are envisaged for use as top sub-cells, and are described below.

The primary focus of the bulk of this dissertation is in realising efficient series interconnects using novel materials that can be applied to tandem hybrid DSSC/BHJ solar cells. Specifically, the interface with spiro-OMeTAD

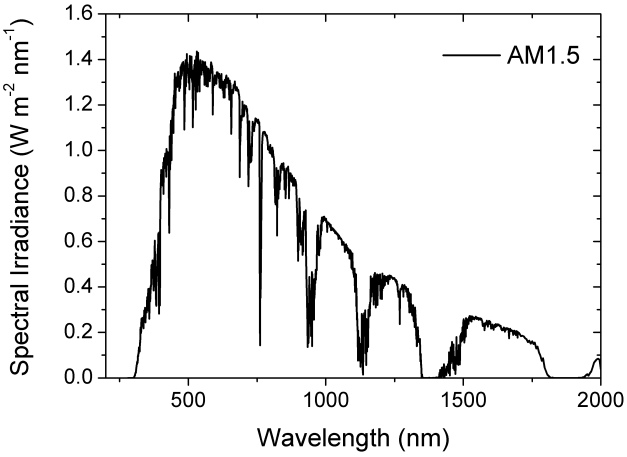

Figure 1.5: Standardized spectrum of solar radiation reaching the earth's surface accounting for absorption in the atmosphere, known as Air Mass 1.5 (Data from NREL [29]).

will be examined, and new materials used to improve hole extraction from DSSCs. By including modifications that will both increase hole and inhibit electron collection at the hole transporter/cathode interface not only will gains be made in the efficiency of single junction DSSCs, but combination with a second sub-cell and accompanying electron extraction layer should enable effective tandem solar cell operation.

1.2.3 Bulk Heterojunction Solar Cells

The first solar cell using the junction between two different organic semiconductors to generate photovoltage was reported in the 1980s by Tang. [32] This used a bilayer of photoactive molecules to generate charge — the most efficient cells today use a primary photoactive component and a second component to enable efficient charge separation. Often polymers that will also

provide a good charge transport medium are used to harvest sunlight, such as poly(3-hexylthiophene) (P3HT), which absorbs strongly over much of the visible spectrum. As with dye-sensitized solar cells photoexcitation results in tightly bound excitons — $\epsilon_r \approx 3$ in the case of P3HT — so charge dissociation must be given a helping hand. [33] A junction is made with a second semiconductor with lower HOMO and LUMO levels, such as the fullerene derivative [6,6]-phenyl C_{61} butyric acid methyl ester (PCBM). Bound excitons diffuse through the absorber medium until encountering an interface between the different semiconductors, where electrons are transferred to the lower LUMO level of the second material. Hence the two components are known as the electron acceptor and donor. Because the HOMO level of the acceptor is also lower than that of the donor, the hole stays on the donor allowing for spatial separation of the charge carriers.

The exciton diffusion length in the polymers is typically on the order of 10nm (reported as 8.5±0.7nm for P3HT, [34]), yet to absorb the majority of incident photons with wavelengths to which the polymer is sensitive the films must be hundreds of nanometres thick. [8] If a simple bilayer junction was made then the vast majority of excitons would recombine before encountering the interface, resulting in very small external quantum efficiency (the ratio of photons incident on the device per unit time to the number or electrons extracted from the device per unit time). To reconcile these competing length scales the two components are blended together, distributing the interface between donor and acceptor materials throughout the bulk of the active layer. In P3HT:PCBM bulk heterojunction cells the length scale of regions of each material in a film hundreds of nanometres thick can be made around

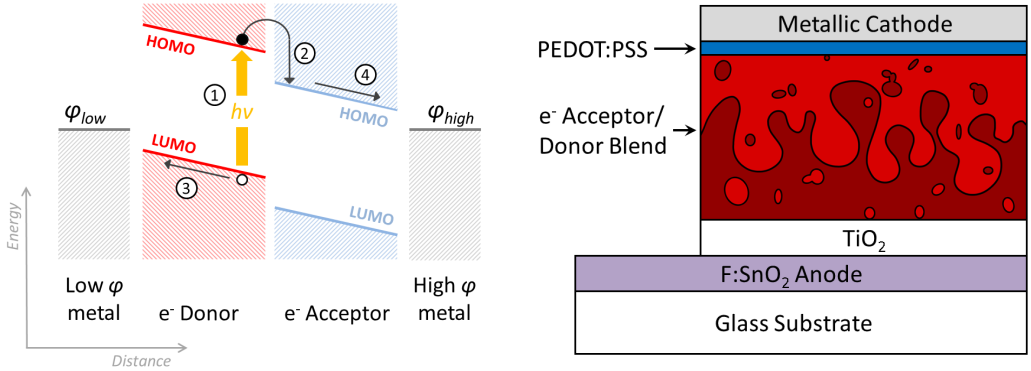

(a) (b)

Figure 1.6: BHJ solar cell operation and structure. 1.6a) Illustrative energy level diagram for a bulk heterojunction solar cell with inverted architecture outlining key processes for charge generation and transport as discussed in the text: 1. Electron donor material excitation by above-band gap radiation, resulting exciton diffuses until either recombination occurs or it encounters a donor/acceptor interface; 2. Charge dissociation through electron injection into acceptor material LUMO; 3. and 4. electric field due to difference in anode and cathode work functions separates charge carriers and pushes them towards electrodes. 1.6b) schematic showing device architecture for a typical BHJ solar cell with inverted architecture.

the exciton diffusion length, ensuring a high proportion of charge dissociation and good light absorption. The disadvantage of this method is that there are typically no guarantees that from any given point in the bulk of the active layer a continuous path to the desired electrode will exist in either semiconductor, increasing the likelihood of recombination before the charge can be extracted.

Once dissociated, charge carrier separation and transport to the appropriate electrode is governed by an electric field between the terminals. This is introduced by using a high work function cathode and lower work function anode. [33] The standard device architecture has the cathode coated onto a transparent conductive substrate, followed by the blended donor/acceptor active layer and the anode on top. DSSCs are fabricated such that holes are collected from the exposed top surface and electrons from the bottom surface, covered by a glass substrate. If a BHJ sub-cell is to be processed on top of a solid-state DSSC for use in a tandem device it must have an inverted architecture, that is to say its anode must be coated first on top of the recombination layer and then the active layer and cathode. Such cells have been reported using fluorine-doped tin oxide (FTO)/TiO_2 anodes and poly(3,4-ethylenedioxythiophene):poly(styrene-sulfonate) (PEDOT:PSS)/silver cathodes. [35] A schematic illustrating the structure and the physical processes resulting in solar cell operation of an inverted BHJ solar cell is shown in figure 1.6.

The fabrication of such solar cells typically does not require heating steps above 150°C in temperature, indeed some donor/acceptor combinations require no heating above room temperature as described in chapter 2, and as with DSSCs, the active components can be processed from solution. These

properties, in addition to the range of donor materials and their varied absorption characteristics, make polymer bulk heterojunction solar cells realistic candidates for inclusion in DSSC/hybrid tandem devices. Importantly, BHJ absorber materials exist that are able to harvest some of the many solar photons of near infrared wavelengths (figure 1.5), a spectral region for which efficient dye molecules do not exist.

Chapter 2

Experimental methods

2.1 Standard Device Fabrication

Unless otherwise stated, solar cell fabrication was carried out according to the following protocols.

2.1.1 DSSC fabrication

The transparent anode comprises of glass coated in FTO of 7Ω/□ sheet resistance (supplied by Pilkington). Though FTO is slightly inferior to ITO (as is often chosen for organic photovoltaics) due in part to its high surface roughness, it is considerably cheaper and thus more appropriate considering the long term objective to make these devices as economical as possible. Selected regions of FTO were etched away chemically using zinc powder and 2M hydrochloric acid (both from Sigma Aldrich) to produce the desired electrode pattern (see figure 2.1). During characterisation gold contact pins are pressed against the electrodes and in some instances there is a risk that the

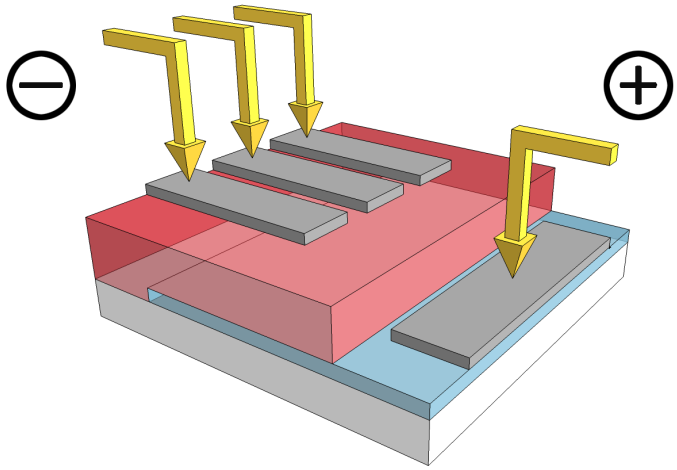

Figure 2.1: DSSC electrode schematic, not to scale. Fluorine-doped tin oxide is represented by blue regions, active layer (TiO_2, dye and hole transporter) by red regions. Grey represents silver contacts: three 3mm wide cathodes contacting spiro-OMeTAD and one common anode contacting the FTO. Gold represents pins for connection to external circuitry. Note the etched region beneath contacts to cathodes to avoid potential shorts.

pins may push right through the cathodes into the active layer — the etched areas are positioned directly below the points of contact to the cathode to remove a possible shorting path through the cell. After etching, the substrate is washed with 2% Hellmanex soap (supplied by Sigma Aldrich) by volume in water, followed by rinsing with deionized water, then acetone and ethanol (both from Sigma Aldrich). Substrates were then treated with oxygen plasma for 10 minutes to remove any remaining organic residue and improve surface wettability.

A compact layer of TiO_2 to block hole transporter material coming into contact with the FTO was deposited by aerosol spray pyrolysis — 5ml of 9vol.% titanium diisopropoxide bis(acetylacetonate) (Sigma Aldrich) in ethanol was sprayed from an atomiser using air as the carrier gas on 11.2cm×

11.2cm substrates held at 250°C on a hotplate. The mesoporous titania structure was created by depositing an anatase TiO_2 nanoparticle paste (Dyesol, 18NR-T) by screen printing, and then calcining the film at 500°C in air. Resulting structures were around 1.8μm in thickness. It was typically at this stage that the substrates were cut into the 1.4cm×1.4cm squares that would become individual test devices. The substrates were then immersed in a bath of $TiCl_4$ (Sigma Aldrich) solution (15mM in water) at 70°C for one hour, then rinsed with deionized water and dried. To complete the electron transporting component, the substrates were again heated to 500°C for a further 45 minutes, before being allowed to cool to 70°C.

The default sensitizer used in the following experiments was the indoline dye D102, supplied by Chimecrea Inc. (though this is by no means the most efficient dye available, it provides a useful control against which to analyse the effects of the experiments reported herein). [36] D102 was dissolved at a concentration of 0.1mg/ml in a 1:1 mixture by volume of acetonitrile and tert-butanol (Sigma Aldrich). Substrates at 70°C were immersed in a bath of dye solution for 1 hour, then rinsed with acetonitrile to wash off any dye not adsorbed to the surface of the TiO_2.

To make the hole transporter solution, spiro-OMeTAD (Lumtec) was added to chlorobenzene and agitated until completely dissolved at 0.09M. To increase the conductivity of the HTM standard additives were used — for every 1ml of chlorobenzene used, 41.1μl/ml of a pre-prepared lithium salt solution was added (Li-TFSI; 170mg/ml of lithium bis(trifluoromethylsulfonyl)-imide in acetonitrile, Sigma Aldrich) and 9.59μl/ml of distilled 4-tert-butyl pyridine (TBP, Sigma Aldrich). [37] Hole transporter was deposited via spin

coating immediately after sensitization was complete: 25μl of solution was deposited onto each 1.4cm×1.4cm substrate, which were then rotated at 1000RPM for 45 seconds to dry the films.

Silver contacts 150nm thick were thermally evaporated under vacuum to complete the devices, the electrode pattern being defined by brass shadow masks. DSSCs were left in air for one day prior to testing.

2.1.2 BHJ solar cell fabrication

FTO glass anodes and TiO_2 hole blocking compact layers were prepared as described above for DSSCs. The desired active layer was then processed on top as described below, and 150nm thick silver electrodes were evaporated using the same pattern and process as for DSSCs.

P3HT:[60]PCBM cells: a one to one blend of regioregular poly(3-hexylthiophene) (P3HT, Rieke Metals) and [6,6]-phenyl C_{61} butyric acid methyl ester ([60]PCBM, Solenne BV) by weight was dissolved at 50mg/ml in chlorobenzene. This was spin cast at 1000RPM for 1 minute yielding a film approximately 300nm thick, followed by annealing at 150°C for 10 minutes to improve the film morphology — this has been shown to increase nanoscale crystallinity and phase segregation between polymer donor and fullerene acceptor, improving charge separation. [38]

PCPDTBT:[70]PCBM cells: Poly[2,1,3- benzothiadiazole-4,7-diyl[4,4-bis-(2-ethylhexyl)-4H-cyclopenta[2,1-b:3,4-b']dithiophene-2,6-diyl]] (PCPDTBT, 1-material) and [6,6]-phenyl C_{71} butyric acid methyl ester ([70]PCBM, Solenne BV) were blended one part polymer to two parts PCBM by weight, and dis-

solved at 30mg/ml in chlorobenzene. Again films cast from solution without modification have a less than ideal morphology for charge separation and transport, however for PCPDTBT thermal annealing shows no improvement in device performance — instead an additional solvent can be mixed into the casting solution that preferentially dissolves one component over the other. [39] To this end, a stock solution of 11% octane dithiol (Sigma Aldrich) in chlorobenzene by volume was prepared, of which 25μl were added to every 100μl of blend solution. This was then spin cast at 1000RPM for 1 minute. The author wishes to acknowledge the work of James Edmands in optimising PCPDTBT:[70]PCBM fabrication that resulted in this protocol, during his time as a summer student co-supervised by the author and Dr Henry Snaith.

It should be noted that poly(3,4-ethylene-dioxythiophene):poly(styrene-sulfonate) (PEDOT:PSS) was not used in BHJ devices, as solutions (supplied by Clevios) would not wet the surface of the polymer blend (numerous attempts were made, adjusting the solution solvent content and adding various amounts of surfactant following Baek et al., but without success), and it is believed that for this reason device performance for P3HT:PCBM cells is markedly poorer than reported in reference [35].

2.1.3 Mesoporous aluminium oxide synthesis

Mesoporous films of insulating material were required for a number of uses in the experiments described in this thesis. Aluminium oxide is one suitable candidate for this purpose — to make a paste suitable for doctor blade coating the following recipe was used: 25.9ml of 20% dispersion by weight

of 50nm Al_2O_3 nanoparticles (Alfa Aesar) was added slowly to 55.6ml of butoxyethanol (Sigma Aldrich) whilst stirring at room temperature. A rotary evaporator was used to remove the water, after which the mixture was diluted two parts to one with ethanol. To this a prepared solution of hydroxypropyl-cellulose (2g of cellulose, Sigma Aldrich, in 25.35ml of ethanol) was added whilst stirring. Once the components were well mixed, ethanol was removed using a rotary evaporator until the paste started to gel. The resulting stock was diluted to the required consistency for each purpose with ethanol, and deposited by doctor blading. As with films of mesoporous TiO_2, the films were baked at 500°C, burning off the solvents and cellulose binder and sintering the nanoparticles together.

2.2 Device and Material Characterisation

2.2.1 Current-Voltage Measurements

A number of key quantities commonly used to describe the performance of solar cells can be extracted from current density-voltage measurements taken over the voltage range in which devices generate a net current when under solar illumination (a generic example of such a plot is shown in figure 2.2), namely the short-circuit current density J_{SC}, the open-circuit voltage V_{OC}, the fill factor FF, and the power conversion efficiency η (PCE). Fill factor is a measure of the quality of rectification and relates J_{SC} and V_{OC} to the

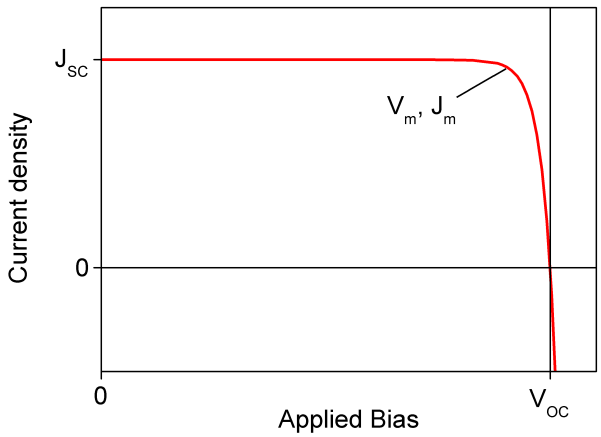

Figure 2.2: An example current density-voltage curve illustrating key values discussed in the text.

maximum power density output of the cell, $J_m \times V_m$:

$$FF = \frac{J_m V_m}{J_{SC} V_{OC}}. \tag{2.1}$$

PCE is defined as

$$\eta = \frac{J_{SC} V_{OC}}{P_S} \times FF \tag{2.2}$$

where P_S is the power density of radiation incident on the device.

It is possible to model a solar cell with the equivalent circuit shown in figure 2.3. [8] A series resistance R_s describes resistance to current flow in the bulk of the cell and the contacts, a shunt resistance R_{sh} in parallel with the cell is used to describe leakage current either through the device via shorting paths or at contacts where carriers of the wrong charge can be collected. The effects of having large R_s or small R_{sh} on a current-voltage curve are shown in figure 2.4. Thus the shape of curve can hint at the electronic processes

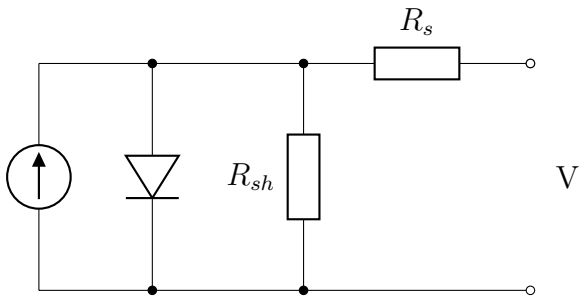

Figure 2.3: Equivalent circuit for a solar cell. A current source and diode in parallel provide a description of the ideal case under illumination — the parasitic shunt R_{sh} and series R_s resistances model the non-ideal behaviour seen in real systems. [8]

that may be reducing the fill factor for a given solar cell.

Given the emphasis on power conversion efficiency in the field of photovoltaic research, its accurate determination is of great importance. Recent studies demonstrate that it is possible for significant error to be introduced in the current density recorded (and hence the efficiency calculated) through incorrect measurement. The active area of each device must be well defined — in the past the overlap between electrodes and the active layer has been used, yet charge generated outside this area may also contribute to the current measured. To ensure that charge is only being generated over a known area an opaque optical mask must be used to shield all other parts of the device from illumination. [40] Gevorgyan et al. have shown that even the lamps used to provide solar-spectrum radiation in test environments can have a large variation in intensity over the area they illuminate, affecting the current generated in a particular device. [41] They also point out light produced by most solar simulators is somewhat diffuse — because photons may enter the device at relatively oblique angles, even well masked solar cells

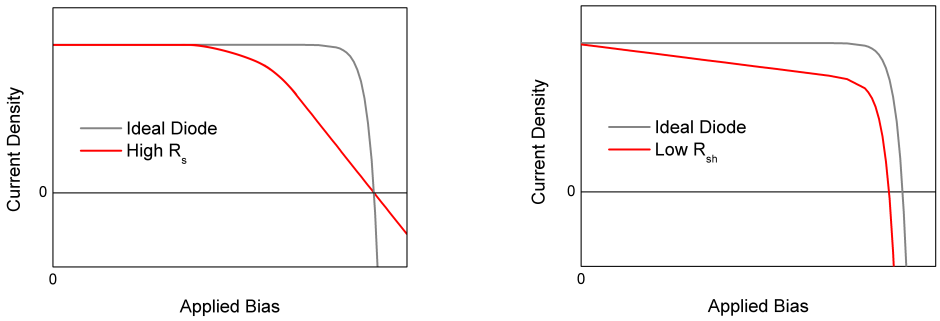

(a) (b)

Figure 2.4: The effect of parasitic resistances on current density-voltage characteristics: 2.4a high series resistance; 2.4b low shunt resistance (after reference [8]).

may end up with an effective active area greater than the area of the mask.

The apparatus used to perform the measurements in the following experiments tries to overcome these potential sources of error. 100mWcm^{-2} air mass (AM) 1.5 illumination was provided by a calibrated ABET class AAB solar simulator. An aperture of 12.6mm in diameter fixed a short distance above the sample stage served to help collimate the light before it reached the devices. The devices themselves have their active areas defined by individual brass optical masks, with apertures very similar in dimension to the silver cathode. Calibration was carried out at the start of each measurement run using a silicon reference diode, the sample stage ensuring that this diode and all test devices were measured at exactly the same position beneath the lamp. Current density as a function of applied voltage was recorded for each cell using a Keithley 2400 sourcemeter.

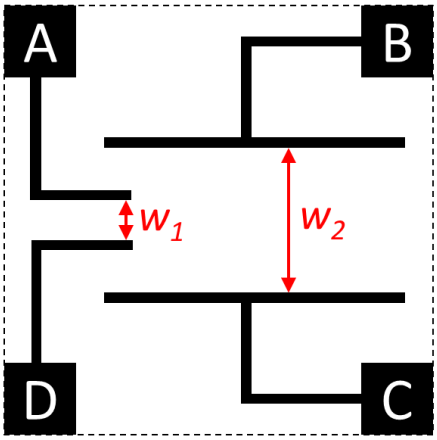

Figure 2.5: Four terminal electrode pattern for measurement of contact resistance. A force voltage is applied across terminals BC, and a response sensed across AD.

2.2.2 Contact resistance and conductivity measurements

When comparing the effectiveness of different electrode materials or electrode/charge extraction interfacial layer combinations, it can be useful to measure the resistance between the electronic contacts and a device. Contact resistance may be extracted from current-voltage curves measured in two and four terminal experiments, and is carried out as follows. Contacts of the desired material are deposited onto the appropriate sample according to a pattern such as that shown in figure 2.5. A voltage V_{force} is applied across the terminals BC and the current I is measured, and from these values the combined resistance of the sample and the contacts may be calculated for ohmic samples. The voltage between the terminals AD, V_{sense}, is also measured — since negligible current flows along the wires connected to A and D

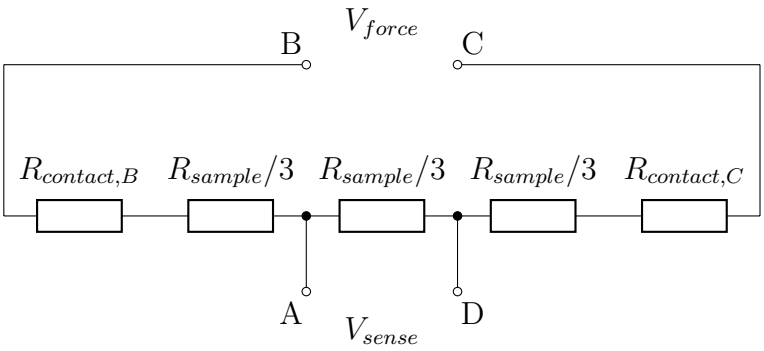

Figure 2.6: Equivalent circuit for contact resistance measurement using electrode pattern shown in figure 2.5 when $w_2 = 3w_1$ and sense electrode channel is parallel and centred with respect to the force channel.

to a first approximation any voltage drop due to contact resistance can be ignored, thus only the resistance of the sample is measured. The configuration used has dimensions $w_2 = 3w_1$, and may be represented by the 5 resistors in series shown in figure 2.6. The sample resistance and total contact resistance can then be given by

$$R_{sample} = \frac{3V_{sense}}{I}, \tag{2.3}$$

$$R_{contact} = R_{contact,B} + R_{contact,C} = \frac{V_{force} - 3V_{sense}}{I}. \tag{2.4}$$

If the thickness of the material being measured is known it is also possible to determine the conductivity σ of the sample using Ohms law, $\mathbf{J} = \sigma\mathbf{E}$ where $\mathbf{J}$ and $\mathbf{E}$ are the current density through the sample and electric field between the electrodes BC respectively. In the case of a sample with uniform cross section this becomes

$$\sigma = \frac{w_2}{R_{sample} l t} \tag{2.5}$$

where l is the length of, and w_2 the separation between the force electrodes

BC, and t is the thickness of the sample being measured, assuming the current density is also uniform throughout the sample.

2.2.3 Pore-filling measurement

An important quantity to measure when comparing HTM deposition techniques is the pore-filling fraction (PFF), defined as the ratio of the volume of the mesoporous network occupied by hole transporter after it has been deposited to the total available volume in the mesoporous network. This has been shown to be closely linked to device performance in a number of studies. [42–46] For the experiments reported here, measurements of pore-filling fraction follow the method described by Docampo et al. and outlined below. [46]. This takes advantage of the fact that a layer of material with different refractive index to its surroundings will have a characteristic interference pattern in its transmission spectrum, the frequency of which is dependent on the thickness of the layer and its refractive index. By looking at the interference spectrum of a film of mesoporous TiO_2 on glass before and after coating with HTM a change in refractive index can be extracted, and from this the volume of HTM in the pores can be calculated.

The refractive index n for a non-dispersive film of thickness d is related to successive maxima in the interference pattern at wavelengths λ_1 and λ_2 by the standard result for light normally incident on the film [47]

$$\frac{1}{2nd} = \frac{1}{\lambda_1} - \frac{1}{\lambda_2}. \tag{2.6}$$

However n is wavelength dependent in dispersive media such as TiO_2 and

spiro-OMeTAD. It has been shown experimentally that even though this is the case, the following expression for an "averaged, effective refractive index" ($n_{av,eff}$ [46]) is a sufficiently accurate approximation for determining the pore-filling fraction:

$$n_{av,eff} \approx \frac{N}{2d_{TiO_2}\left(\frac{1}{\lambda_1} - \frac{1}{\lambda_N}\right)} \tag{2.7}$$

Here N is the total number of maxima observed in the spectra, λ_1 and λ_N are the wavelengths corresponding to the first and last maxima respectively. Substrates without dye or HTM are first measured to determine the porosity of the TiO_2 film — as it is essentially a film of air filled with nominally spherical inclusions of titania it satisfies the conditions of the Bruggeman mean field approximation (equation 2.8), which relates the refractive indices n and volume v fractions of constituent materials in a film of mixed composition to the measured refractive index of the film n_{film}. [48]

$$\sum_i v_i \frac{n_i^2 - n_{film}^2}{n_i^2 + 2n_{film}^2} = 0 \tag{2.8}$$

From this v_{air}, that is the available space before coating for the hole transporter to fill, can be calculated since n_{air} and n_{TiO_2} have known values for a given wavelength. After the substrate has been coated with hole transporter, The resulting film can no longer be described as spherical inclusions of one or more materials inside a bulk of another. Instead a linear approximation

provides a satisfactory approximation for this system [46]:

$$\sum_i v_i' n_i = n_{film}' \tag{2.9}$$

where quantities marked with a prime indicate the value after hole transporter deposition. Docampo et al. demonstrated that sensitization with dye has negligible effect on pore-filling, so to simplify the measurements reported here, no dye was added before depositing hole transporter, leaving just TiO_2, HTM and air components in equation 2.9. At this point the calculations are complicated by the fact that when adding the hole transporter a layer typically forms on top of the TiO_2 as well as infiltrating the pores, known as the capping- or over-layer. This contributes to the change in the refractive index of the sample, but typically it is not possible to separate interference patterns due to the capping layer and those of the rest of the sample. Instead the approximation is made that since the refractive indices of the capping layer and the partially filled TiO_2 are similar, interference between the two can be ignored, yielding the expression

$$\frac{N}{2n_{av,eff}d_{TiO_2} + 2n_{spiro}d_{CL}} \approx \frac{1}{\lambda_1} - \frac{1}{\lambda_2}, \tag{2.10}$$

where n_{spiro} is the refractive index of spiro-OMeTAD, and d_{TiO_2} and d_{CL} are the thicknesses of the TiO_2 film and hole transporter capping-layer respectively. Combining this with equation 2.9 gives

$$n_{film}' = n_{av,eff} = \sum_i v_i' n_i + \frac{n_{spiro}d_{CL}}{d_{TiO_2}} \tag{2.11}$$

From these expressions the volume fraction of hole transporter (v'_{spiro}) and thus the pore-filling fraction can be found:

$$PFF = \frac{v'_{spiro}}{v_{air}}. \tag{2.12}$$

2.2.4 Scanning electron microscopy

Scanning electron microscopy (SEM) was used in some investigations to observe device and device component morphology, and was performed with a Hitachi S-4300 system. Where DSSC cross-section images were required, a diamond scribe was used to score a short line on the active side of the device to aid in cleaving it in two and leaving a clean edge to image beyond the end of the score mark. Samples were prepared by sputtering 3nm of platinum onto the surface being imaged to reduce accumulation of charge when under the electron beam.

Chapter 3

Transition metal dichalcogenide (TMDC) charge extraction interfaces

When compared with inorganic solar cell technologies, solid-state DSSCs typically exhibit poor fill factors, with larger series and lower shunt resistances than their more established counterparts. A variety of factors may contribute to this, but one of particular relevance to the theme of series interconnects is the less than ideal charge extraction from solid-state DSSCs due to imperfect contact electrodes and their interfaces with the semiconductor components. A contact should selectively provide a low resistance route for the extraction of either electrons or holes from the device whilst inhibiting carriers of the opposite charge. This chapter is the first of two examining attempts to improve hole extraction from spiro-OMeTAD in particular, through the use of interfacial layers to alter electronic properties at

the hole transporter/electrode interface. Such layers are envisaged for end use in tandem interconnects when brought into contact with an appropriate electron collection layer upon which a rear BHJ sub-cell may be processed.

The workhorse hole extraction layer for bulk heterojunction solar cells has traditionally been the organic material PEDOT:PSS. It is however acidic and hygroscopic, and creates serious problems with device stability due to its tendency to etch metallic components and introduce water to neighbouring organics. [49, 50] In addition it has been shown to have less than ideal electron blocking properties. [51] The author's own experience has been that PEDOT:PSS is also not ideal for solid state DSSCs, with layers processed on top of spiro-OMeTAD yielding devices that will typically give higher currents but lower fill factors when current-voltage characteristics are scanned for the first time, but significantly poorer currents after subsequent scans and are outperformed by control devices. It has also been noticed that open circuit voltage is slightly lower on average than control devices. An example of this is shown in section 3.2.2 (figure 3.8).

In recent years much work has been done to find other hole extraction materials that have less of an impact on stability. In particular, success has been had using transition metal oxides. [52, 53] Here investigations have been carried out into another class of materials, namely transition metal dichalcogenides (TMDCs). Though general research into this class of materials has been on-going for decades, recently there has been much interest in incorporating TMDCs into electronic devices of many kinds. [54] TMDCs take the chemical form TX_2, where T is a transition metal and X is sulphur, selenium or tellurium. They have a range of electronic properties, and include

metals, semi-metals and semiconductors. [55] Many TMDCs have a structure where a layer of metal atoms arranged in a two-dimensional hexagonal array is covalently bonded to layers of S, Se or Te atoms above and below — successive TX_2 sheets are held together by van der Waals interactions. [55, 56] The surfaces of these structures are chemically inert — a useful property for incorporation in organic and hybrid electronics.

Two such TMDCs are tungsten disulphide (WS_2) and molybdenum disulphide (MoS_2). They exhibit semiconducting behaviour and could be promising candidates for use as hole extraction layers for solid-state DSSCs due to their deep conduction and valance band edges relative to the HOMO and LUMO levels in spiro-OMeTAD (summarised in table 3.1). Indeed they have been used successfully for a similar purpose as hole injection layers in organic light emitting diodes (OLEDs) by Frey et al., and more recently as counter electrodes in liquid electrolyte DSSCs. [56–59] Figure 3.1 illustrates the band bending hypothesised to occur when spiro-OMeTAD and either WS_2 or MoS_2 are brought into contact (not to scale). The degree of band bending will depend on the exact position of the Fermi levels and band edges in each semiconductor. In the case of the TMDC material being *p*-type (figure 3.2a), a spike in potential known as a Schottky barrier is introduced in the LUMO level for spiro-OMeTAD inhibiting electron transfer across the junction (in a DSSC device, this would increase the shunt resistance), whilst a corresponding drop in potential for holes in the HOMO level can make hole extraction into the TMDC more favourable (decreasing series resistance in a device). The situation is different if the TMDC is *n*-type (figure 3.2b) — in this scenario the band bending may be such that a Schottky barrier is

Material	VB/HOMO	CB/LUMO
Spiro-OMeTAD	−5.11eV	−2.05eV
WS_2	−6.22eV	−4.86eV
MoS_2	−5.90eV	−4.73eV

Table 3.1: Band edges/molecular orbital levels of Spiro-OMeTAD and bulk TMDC material relative to vacuum. Data from [61] and [62] (it should be noted however that HOMO and LUMO values can vary largely depending on the measurement method employed).

introduced for holes at the junction, but the TMDC conduction band may become degenerate with the Fermi level. If this occurs the TMDC at the junction becomes metallic and the interface becomes the recombination site with electrons from the external load. Indeed transition metal oxides operating in a similar regime have been shown to be heavily n-type and yet demonstrate good hole extraction. [60] The exact nature of the band profile at the junction between spiro-OMeTAD and either WS_2 or MoS_2 is not known, but in either scenario, the result should be that hole extraction from the DSSC is improved.

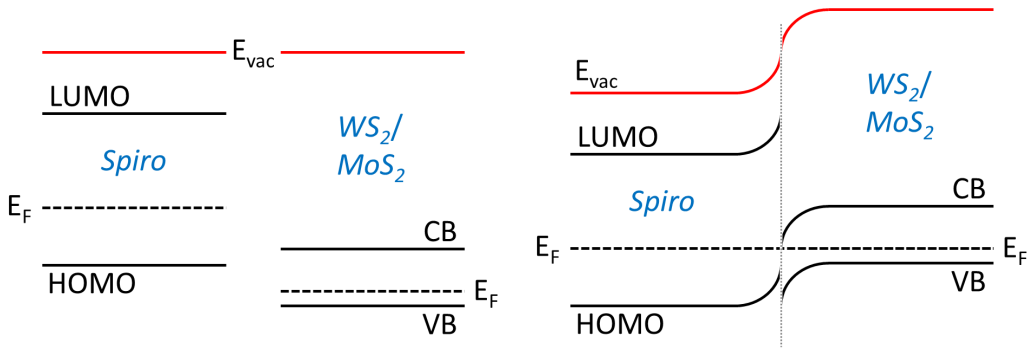

(a) (b)

Figure 3.1: Hypothetical band diagrams (not to scale) for spiro-OMeTAD and WS_2 or MoS_2 in isolation (3.1a) and at a heterojunction (3.1b). Vertical axis represents energy, horizontal represents distance. Note that spiro-OMeTAD with additives will be slightly *p*-type, but the position of the Fermi level within the TMDCs has been drawn arbitrarily, and need not also be *p*-type.

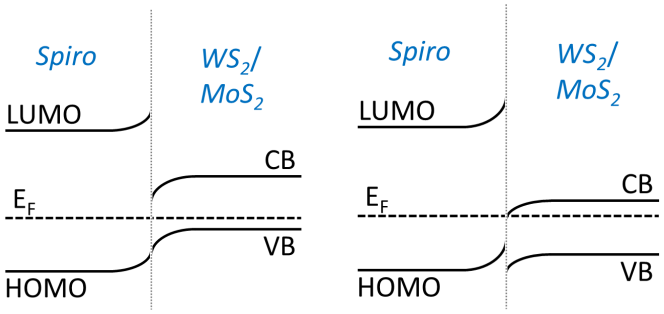

(a) (b)

Figure 3.2: Different band bending scenarios at a spiro-OMeTAD/TMDC junction as described in the text (not to scale). Vertical axis represents energy, horizontal represents distance.

3.1 Experimental details

Device fabrication follows the protocol outlined in section 2.1, using the dye D102. Previous work on OLEDs has used a process mixing p-xylene with a dispersion of TMDC in water — a thin film of TMDC is formed at the solvent/water interface, and a substrate is carefully dipped into the mixture to pick up this layer. As the various organic components in an almost complete solid-state DSSC are sensitive to contact with the solvents involved, this method is impractical. It is also not a technique that is easy to scale up in a commercial production scenario. Instead, dispersions of exfoliated WS_2 and MoS_2 in isopropanol were provided by Valeria Nicolosi[1] having been fabricated according to reference [63]. To briefly summarise their synthesis, mixtures of powdered bulk WS_2 and MoS_2 in isopropanol were placed in an ice bath and ultra-sonicated for two hours to disperse the TMDC, left to settle over two nights, then centrifuged for one hour at 3000 RPM. The supernatant was collected and diluted to a final concentration of 0.1mg/ml. These dispersions lend themselves well to scalable deposition methods that are suitable for use on DSSC components. It is noted that the method used to produce these dispersions preserves the semiconducting properties of the TMDCs — those used by others can result in a metallic transition. [56] TMDC dispersions of 0.1mg/ml concentration were agitated in an ultrasonic bath for 7 minutes before being deposited via aerosol spraying using air as the carrier gas, with the substrates (sensitized photoanodes already coated with hole transporter) on a hotplate at 120°C to evaporate the isopropanol. Though the dispersion

[1]Valeria Nicolosi, ERC Research Professor, Trinity College Dublin

synthesis should yield monolayers of TMDC crystal, it was not guaranteed that deposition in this manner would maintain a two-dimensional form or create regions of bulk material. After cooling, silver cathodes were thermally evaporated onto the devices according to the standard protocol.

3.2 Results and discussion

3.2.1 TMDC film characterisation

Material	Band gap (bulk)	Band gap (2D)
WS_2	1.4eV	1.9eV
MoS_2	1.2eV	1.8eV

Table 3.2: TMDC band gaps for bulk material and for two-dimensional single layers. Data from reference [54].

Absorbance spectra of films of WS_2 and MoS_2 on glass were taken from UV to IR wavelengths (figure 3.3). The long tail off in each spectrum is due to scattering, which is not accounted for in this measurement. The strongest absorption takes place at higher energies in the visible spectrum in both cases. Excitonic peaks are visible in both the spectra at higher energies than the band gaps for the respective bulk TMDC materials, indicating the presence of single-layer crystals with two-dimensional electronic properties (see table 3.2). [54] The single layer band gap values are indicated on the spectra.

The SEM images in figures 3.4 and 3.5 show top down views at various magnifications of films of WS_2 and MoS_2 respectively, sprayed onto glass us-

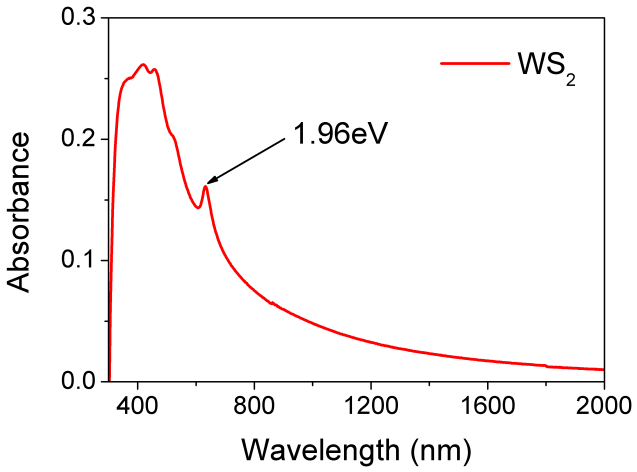

(a)

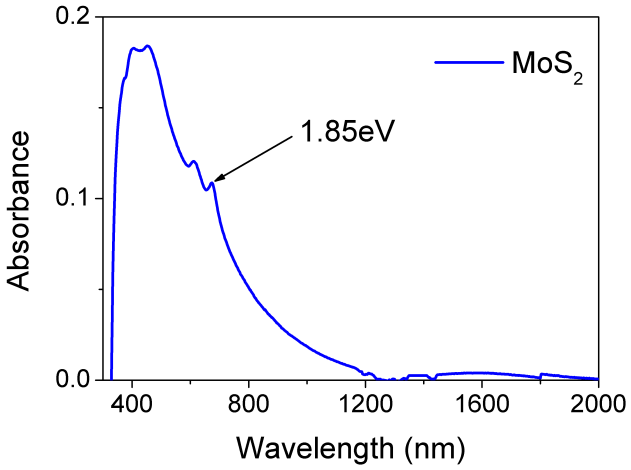

(b)

Figure 3.3: Absorbance spectra of films of WS_2 and MoS_2 deposited on glass according to spray protocol outlined in the text. The energies of the first excitonic peaks are also indicated, and show the presence of single layer TMDC crystals.

ing the protocol described above. It is immediately clear that this deposition method does not result in the formation of smooth and continuous films. Instead, the majority of the material forms rings tens of microns in diameter

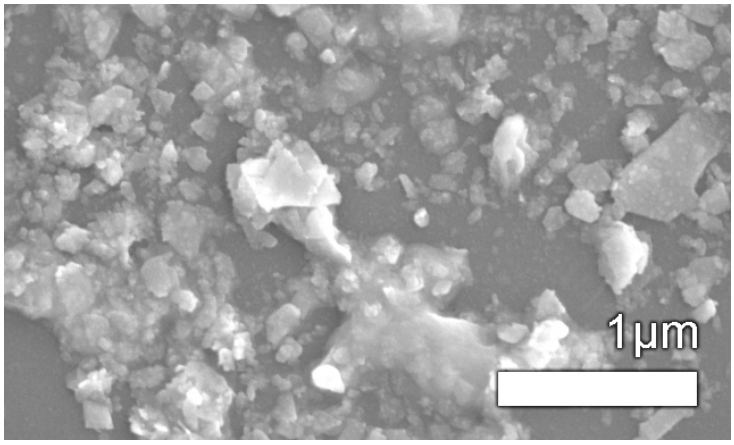

(a)

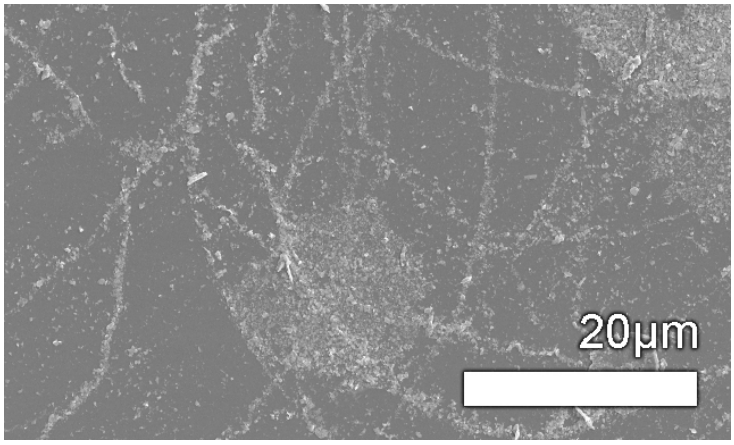

(b)

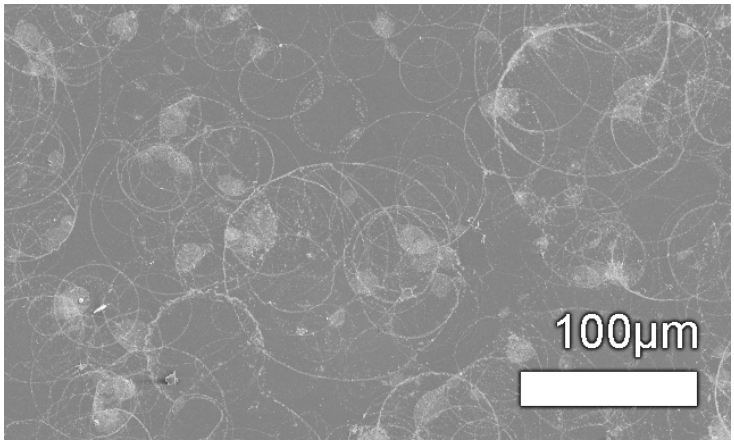

(c)

Figure 3.4: SEM images of WS_2 film deposited by spray pyrolysis as described in the text.

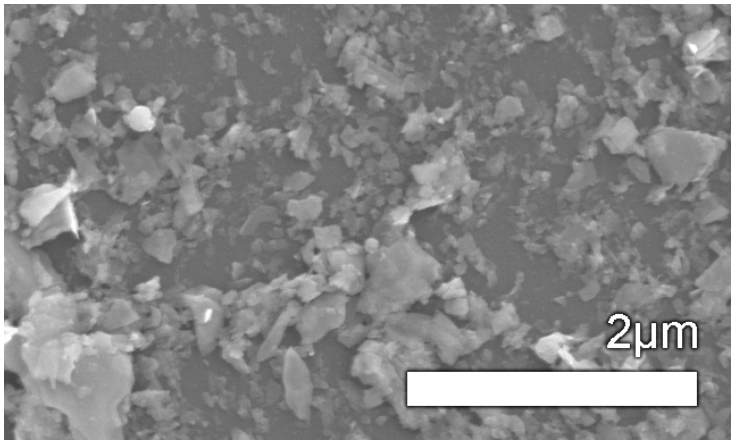

(a)

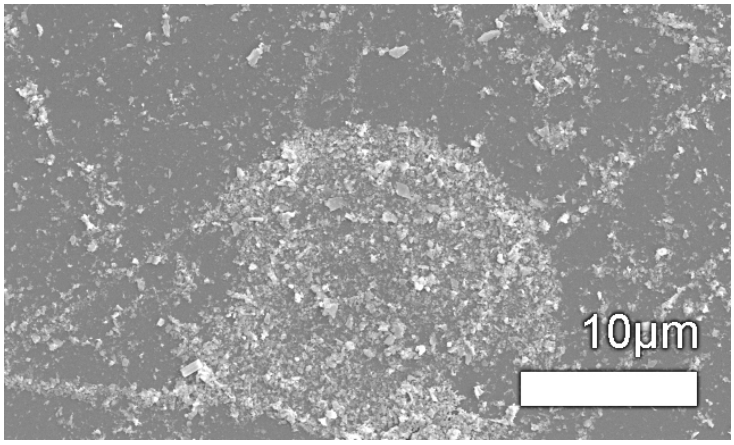

(b)

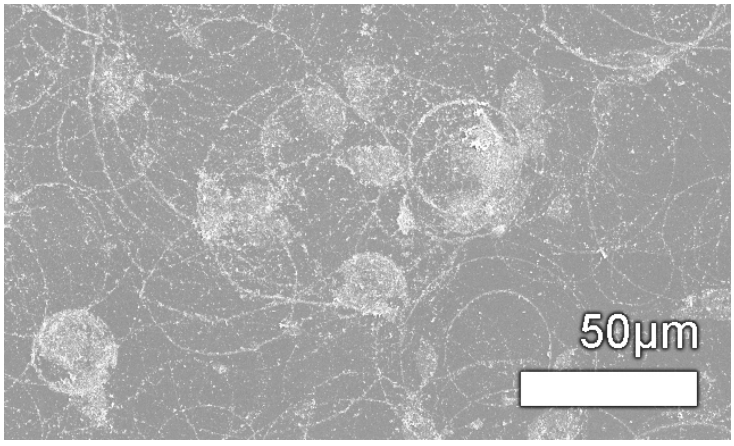

(c)

Figure 3.5: SEM images of MoS_2 film deposited by spray pyrolysis as described in the text.

comprised of TMDC structures with dimensions on the order of hundreds of nanometres leading to a very rough and possibly discontinuous arrangement of material. The implication is that in devices, areas of silver electrode may bypass the TMDC material and contact the hole transporter directly in places. Further images were taken to verify that films formed in the same manner when sprayed onto spiro-OMeTAD as on glass.

3.2.2 Device performance

Performance parameters for control devices (no TMDC) and cells with WS_2 and MoS_2 interfacial layers are shown in figure 3.6. Current density-voltage curves (averaged over all devices in each batch) have been plotted in figure 3.7. Both TMDCs perform well, matching the hope of obtaining higher current and power conversion efficiency. WS_2 devices exhibit higher fill factors than MoS_2 but show a slightly lower average V_{OC}.

Additionally devices using dichalcogenide hole extraction layers do not appear to share the issue of a rapid degradation in performance with those using PEDOT:PSS. As the applied bias was repeatedly scanned over 0-1V, J_{SC}, V_{OC}, fill factor and efficiency varied very little. A comparison between the behaviour of selected example devices using PEDOT:PSS, WS_2 and MoS_2 as hole extraction layers after a set number of scans is shown in figure 3.8 and table 3.3.

In an attempt to further elucidate these data, the contact resistance between silver and films of spiro-OMeTAD or TMDC/spiro-OMeTAD bilayers was measured using the four terminal arrangement described in chapter 1.

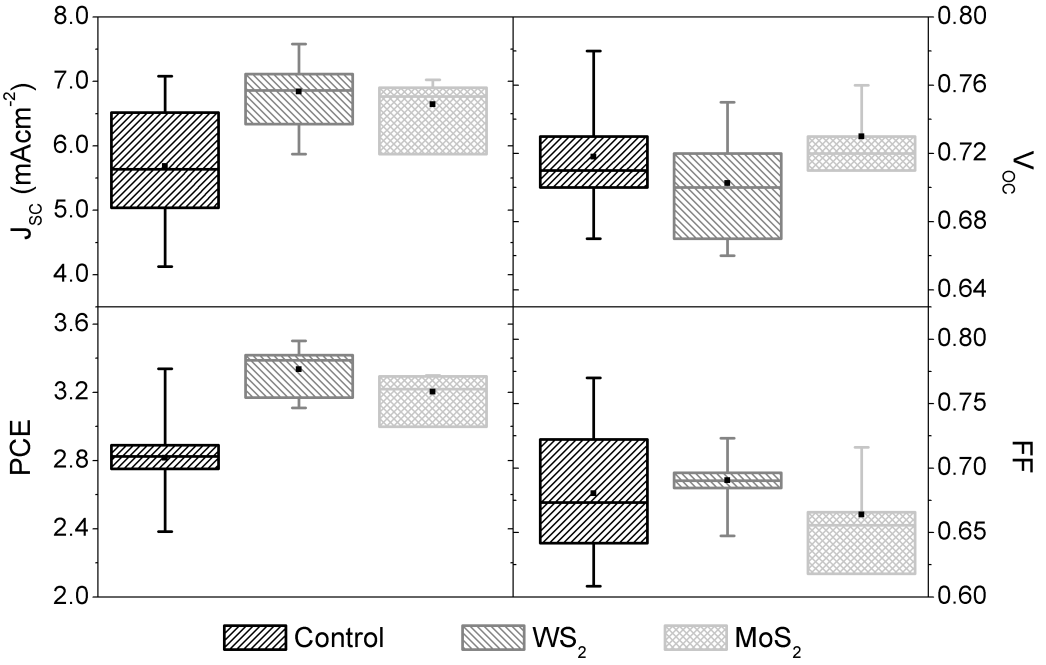

Figure 3.6: Performance parameters of DSSCs with TMDC interfacial layers extracted from current voltage measurements under simulated solar illumination. Box plots showing outlier, upper and lower quartile and median values for short circuit current density J_{SC}, open circuit voltage V_{OC}, power conversion efficiency PCE and fill factor FF. Mean values indicated by black squares. Data set consists of 10 control devices, 8 WS_2 devices and 4 MoS_2 devices.

TMDCs are highly anisotropic, and show a conductivity parallel to the TX_2 planes typically several orders of magnitude greater than the perpendicular direction. [55] It was hypothesised that deposition would not lead to the TMDC crystals all having exactly the same orientation, as seems to be supported by the SEM images in figures 3.4 and 3.5. In this scenario the conductivity of the film is likely to be lower than the value parallel to the TX_2 planes, and could potentially be lower than that of spiro-OMeTAD with additives (2×10^{-5} Scm^{-1}, [37]). If this were the case, a reduced contact re-

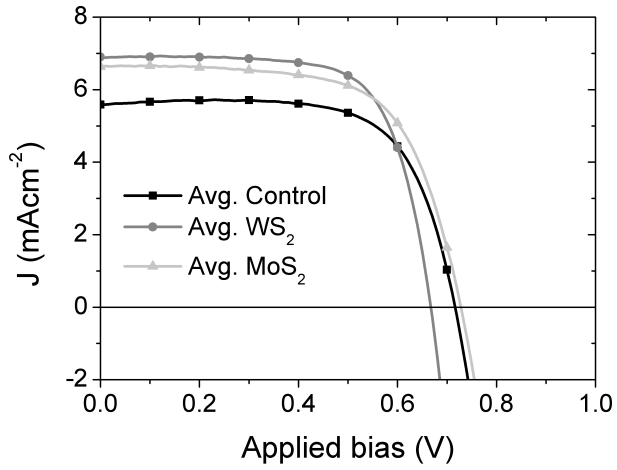

Figure 3.7: Averaged current-voltage curves for DSSCs with TMDC interfacial layers measured under simulated AM 1.5 solar illumination. Data set consists of 10 control devices, 8 WS_2 devices and 4 MoS_2 devices.

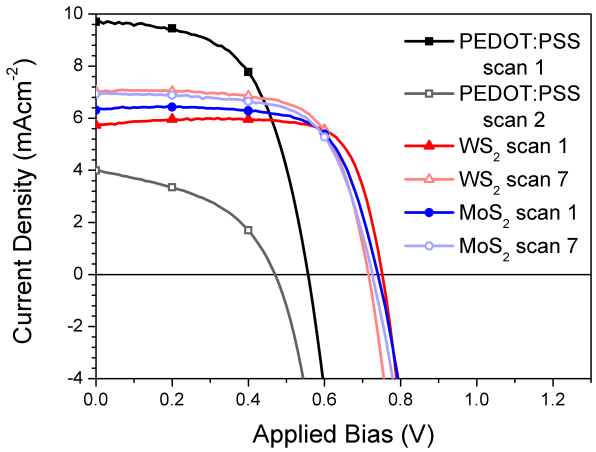

Figure 3.8: Example current density-voltage curves for DSSCs using PEDOT:PSS, WS_2 and MoS_2 hole extraction layers, showing the response of the same cells when biased from 0V to 1V for the first and seventh times.

sistance and a similar sample resistance for a spiro-OMeTAD/TMDC film when compared to spiro-OMeTAD by itself would be indicative of improved contact between the hole transporter and the electrodes. If however the sam-

Hole extraction layer	Scan number	J_{SC} ($mAcm^{-2}$)	V_{OC} (V)	PCE (%)	FF
PEDOT:PSS	1	9.70	0.56	3.10	0.57
	7	4.00	0.47	0.85	0.45
WS_2	1	5.73	0.75	3.31	0.74
	7	7.03	0.72	3.41	0.67
MoS_2	1	6.31	0.74	3.25	0.69
	7	6.93	0.73	3.29	0.65

Table 3.3: Example device performance characteristics for DSSCs using PEDOT:PSS, WS_2 and MoS_2 hole extraction layers, showing values for the same cells when biased from 0V to 1V for the first and seventh times.

ple resistance decreased significantly with the addition of a TMDC film it would be clear that the conductivity of the hole extraction layer is higher than that of spiro-OMeTAD. In this case the TMDC is transporting the majority of the charge and little could be said about the quality of the contact to the hole transporter beneath.

From experience it is difficult coat spiro-OMeTAD with Li-TFSI and TBP additives directly onto glass without the casting solution de-wetting during spin coating. Instead, mesoporous Al_2O_3 600nm thick (see section 2.1) was prepared on glass via spin coating, giving an insulating porous surface which the hole transporter is able to wet. Spiro-OMeTAD was spin coated in the usual way giving a configuration somewhat similar to that of an actual device. Layers of WS_2 or MoS_2 were then deposited as described above and silver electrodes in the four terminal pattern (see figure 2.5) were evaporated on top. The sample structure described is shown in figure 3.9.

Averaged contact resistances for WS_2 and MoS_2 on spiro-OMeTAD are shown in figure 3.10, along with uncoated spiro-OMeTAD on which neat

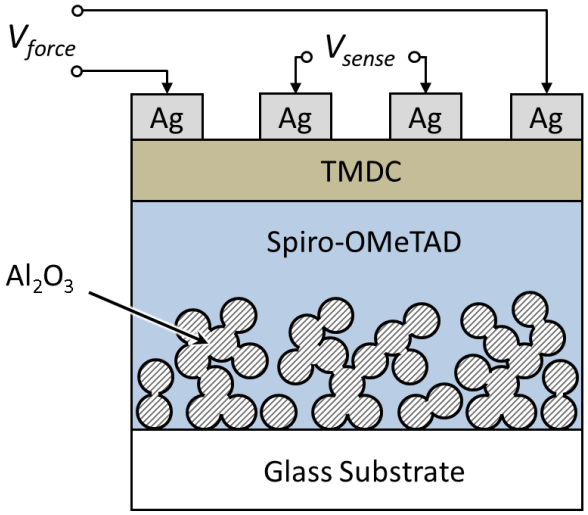

Figure 3.9: Cross sectional Structure of TMDC contact resistance samples.

isopropanol (IPA) was sprayed according to the same procedure as TMDC deposition (to ensure any positive effects were indeed due to the TMDCs themselves, and not to any possible change in HTM morphology brought about through processing), and uncoated spiro-OMeTAD that received no further treatment. The data are difficult to interpret however, with large discrepancies between repeat samples resulting in significant uncertainty in the final value. It is possible to conclude that there is no large effect when adding the TMDC films (or upon treatment with sprayed isopropanol). This is perhaps consistent with the knowledge that the films are very likely discontinuous, and at the very least have a large surface roughness that may result in the very narrow silver electrodes used (50 μm wide) being discontinuous themselves — the electrodes may be predominantly contacting spiro-OMeTAD directly in all cases, but to different extents between samples.

Given the morphological shortcomings of these TMDC films, it is surpris-

ing that they should have such a clear effect on device performance. It is not unreasonable to surmise that refinement of the deposition process could yield more significant gains in DSSC efficiency. The obvious first step was to vary the quantity of material laid down during spray pyrolysis. MoS_2 devices were made as before, but spraying down material in 20, 40, 60 and 100 separate coats (60 coats were used previously). The performance parameters and averaged current density-voltage curves can be found in figures 3.11 and 3.12 respectively. Whilst it is clear that with thicker layers of TMDC the current that can be obtained from a cell increases, it is at the cost of both fill factor and open circuit voltage. The current response of the cells in the dark shows this poor rectification is consistent with a significant decrease in shunt resistance — this is most likely an artefact of the small area cell configuration used and the possible occurrence of shorting paths from the silver to the FTO via the thick layer of TMDC. It therefore seems likely that aerosol spray deposition of this form is not ideal, and a method that allows thinner, continuous films to form would be preferable.

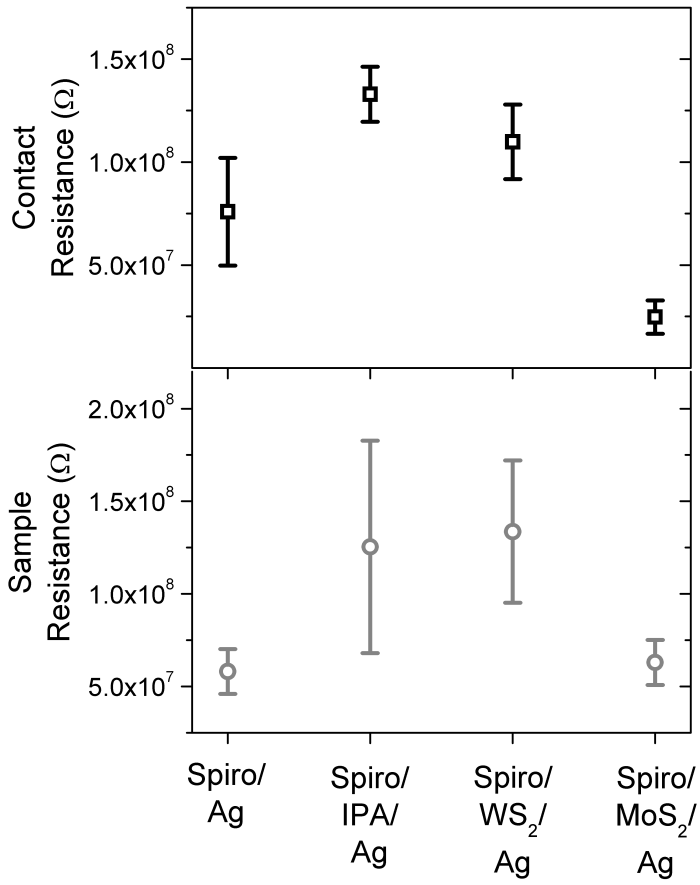

Figure 3.10: Sample and contact resistances calculated using equations 2.3 and 2.4 for untreated spiro-OMeTAD, for WS_2 and MoS_2 interfacial layers on spiro-OMeTAD, and for spiro-OMeTAD subjected to isopropanol-only spray procedure (IPA), as measured using the four-point probe setup described in the text.

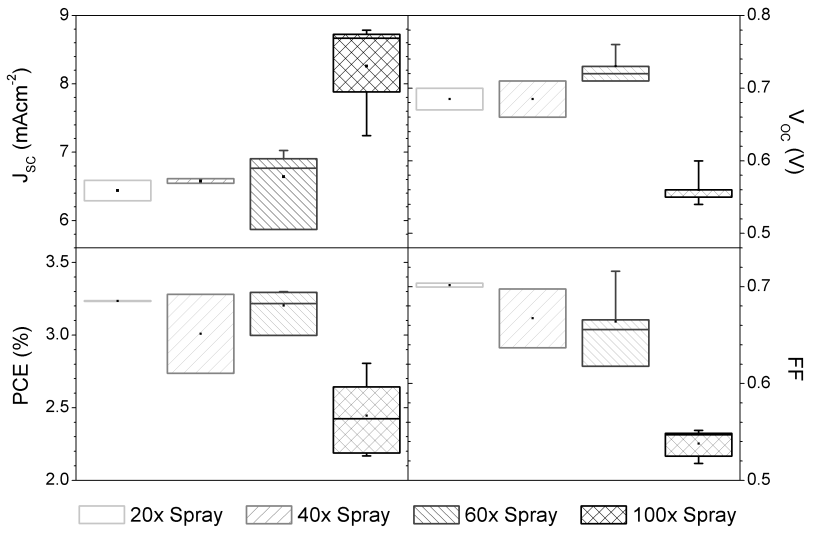

Figure 3.11: Device performance with changing thickness of MoS_2. Box plots for varying numbers of spray coats showing minimum, maximum, upper and lower quartile and median values. Mean values shown as black squares. Data set comprises 2 devices sprayed 20 times, 2 sprayed 40 times, 4 sprayed 60 times and 4 sprayed 100 times.

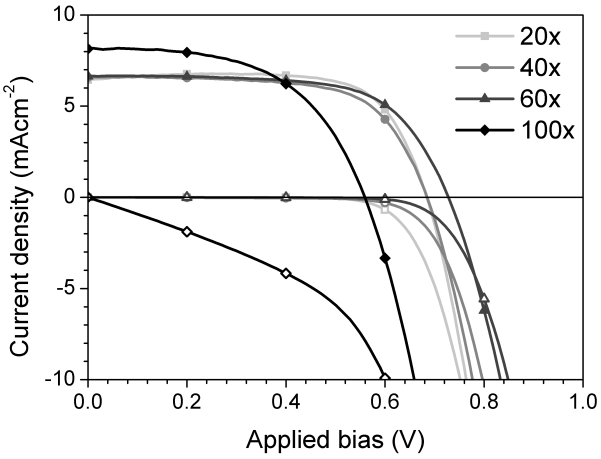

Figure 3.12: Averaged current density-voltage curves as a function of different numbers of MoS_2 coats. Data set comprises 2 devices sprayed 20 times, 2 sprayed 40 times, 4 sprayed 60 times and 4 sprayed 100 times.

3.3 Conclusion

It has been demonstrated that through the addition of interfacial tungsten or molybdenum disulphide layers, deposited using simple and scalable techniques, device performance in solid-state DSSCs can be markedly improved and is postulated to be due to better hole extraction from spiro-OMeTAD to the cathode. These improvements come despite poor film formation by aerosol deposition, suggesting that optimisation of coating process could significantly improve device performance. Possible routes for achieving this might be through developing a dispersion of TMDC with suitable properties for spin coating or doctor blade coating (for example Li et al. have reported doctor blade coated porous WS_2 films [59]), or perhaps through ultrasonic spray deposition.

These materials also have good potential for use as tandem interconnect components. The combination of hole extracting/electron inhibiting properties, having chemically inert surfaces and the ability to be processed from solution without requiring high temperatures are all ideal qualities for combination with an electron extraction component to form a recombination layer.

Chapter 4

Doped organic semiconductor nanoparticle dispersions

Chapter 3 discussed the use of hole extraction layers composed of semiconductor materials that were completely different chemically to the bulk hole transporter. In the case of inorganic tandem and multiple junction photovoltaics, efficient hole/electron extraction layers (and the combination of both in the case of series interconnects) are typically achieved through spatial changes in dopant level in the bulk semiconductor to promote the collection of one charge carrier species whilst inhibiting the other. [8] In this second chapter on charge extraction interfaces an alternative route to improve collection of holes from a DSSC is presented, using a heavily doped layer of spiro-OMeTAD as an interfacial layer to make an architecture analogous to that used in inorganics. Adding highly *p*-type spiro-OMeTAD before the silver electrode will have a similar effect to adding tungsten or molybdenum disulphide — band bending will make it energetically preferable for elec-

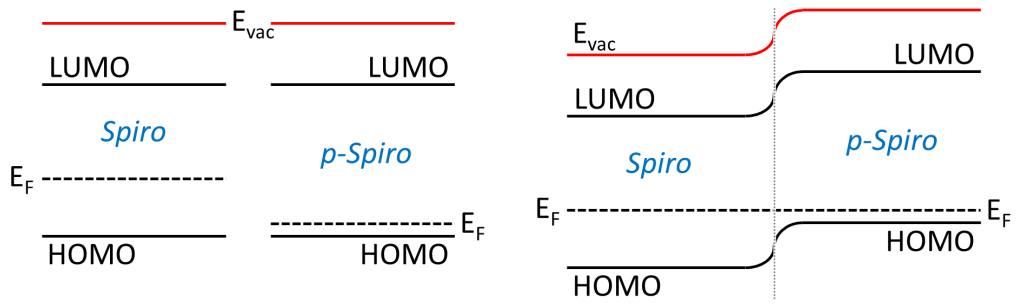

(a) (b)

Figure 4.1: Band diagrams (not to scale) for spiro-OMeTAD both lightly and heavily *p*-type doped in isolation (4.1a) and at a heterojunction (4.1b). Vertical axis represents energy, horizontal represents distance.

trons to stay within the bulk and for holes to transfer to the highly *p*-type interfacial layer (see figure 4.1).

In practice, such an interfacial layer is hard to achieve. A second layer of spiro-OMeTAD cannot simply be coated on top of the first, as the solvent carrying the additional material will re-dissolve any HTM film it comes into contact with. It is possible however to circumvent this problem though the use of nanoparticle dispersions. Landfester and co-workers demonstrated that mini-emulsion processing can be used to create nanoparticles from organic polymer semiconductors that can then be dispersed in a solvent in which the organic material is insoluble. [64] The process is illustrated in figure 4.2 and is carried out as follows: An organic polymer material that is highly insoluble in water is dissolved in a solvent that is both immiscible with, and has a lower boiling point than water. This is added to a solution of surfactant in water, and agitated using ultrasound to create a mini-emulsion of droplets 50-500nm

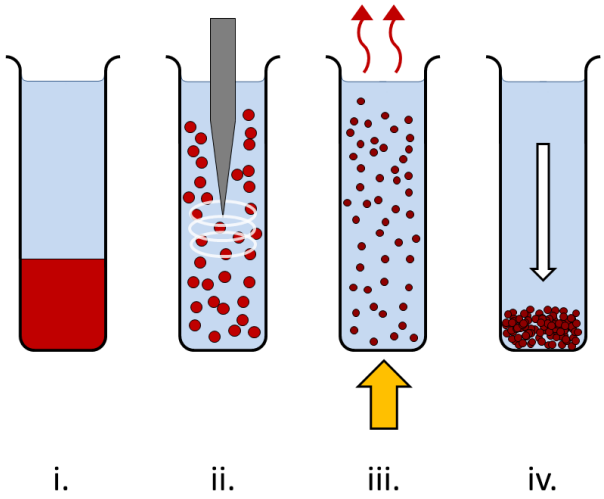

Figure 4.2: Nanoparticle dispersion synthesis: i) aqueous solution of surfactant (light blue phase) added to immiscible solution containing organic semiconductor (red phase); ii) probe providing high amplitude ultrasound creates emulsion of nano-droplets of dissolved semiconductor; iii) heat applied to evaporate non-aqueous solvent; iv) resulting dispersion centrifuged to separate nanoparticles.

in diameter containing the polymer suspended in the surrounding water. The surfactant acts to stabilize the droplets, and the mixture is heated at the boiling temperature of the organic solvent. The organic solvent evaporates leaving a dispersion of nanoparticles in the surfactant solution.

This technique has been applied to the molecular semiconductor spiro-OMeTAD. By re-dispersing the nanoparticles in isopropanol (a poor solvent for many organic semiconductors, including spiro-OMeTAD) it is possible to spin coat consecutive layers of HTM without affecting organic films underneath. In an analogous way, electron extraction at the anode in organic polymer bulk heterojunction devices can potentially be improved through the use of a doped interfacial layer. To this end *n*-type dispersions of the

electron acceptor [60]PCBM were also fabricated.

4.1 Experimental details

4.1.1 Synthesis

Spiro-OMeTAD nanoparticles: On addition of Li-TFSI salts when preparing solutions of hole transporter (see section 2.1), spiro-OMeTAD becomes oxidized and behaves as a *p*-type semiconductor. In order to form a junction as described above it is necessary to dope the spiro-OMeTAD that is to form the interfacial layer still further through reaction with a suitable oxidizing agent. For this purpose nitrosyl tetrafluoroborate ($NOBF_4$) was used. For the nanoparticle dispersion, a solution of spiro-OMeTAD at 50mg/ml was prepared as described in section 2.1, scaling the Li-TFSI and TBP additive quantities according number of moles of hole transporter, though importantly using chloroform in place of chlorobenzene. $NOBF_4$ was then added at 100mol% concentration with respect to spiro-OMeTAD. The surfactant sodium dodecyl sulphate (SDS) was dissolved at 3mg/ml in water. The solutions were added 2.83:10 (HTM solution:surfactant solution) by volume and stirred until well mixed, placed in an ice bath, and an ultrasonic probe used to form the mini-emulsion. The vial containing the emulsion was raised to 70°C inside an aluminium sheath to ensure uniform heating whilst stirring for 3 hours, after which the chloroform had evaporated. The nanoparticles were removed after centrifuging the mixture at 7000 RPM overnight and were re-dispersed in isopropanol.

PCBM nanoparticles: [60]PCBM was dissolved in chloroform at 5mg/ml. This was *n*-type doped using the reducing agent 1,3-Dimethyl-2-phenyl-2,3-dihydro-1*H*-benzo-imidazole (DMBI) at 100mol% concentration with respect to the PCBM. [65] DMBI is sensitive to water, and was added to the PCBM solution under a nitrogen atmosphere. A solution of SDS was prepared as for *p*-type spiro-OMeTAD and subsequent synthesis steps were carried out as described above.

4.1.2 Device fabrication

DSSC fabrication followed the standard protocol up to electrode evaporation (sec. 2.1). The doped nanoparticles were spin coated from IPA dispersions at 1500RPM for 45s, then heated at 120°C for 10 minutes to drive off any remaining solvent. It is noted that the glass transition temperature of spiro-OMeTAD is 125°C, so this heating step may also help to bond the *p*-spiro-OMeTAD nanoparticles into a more robust structure. [61] In the case that further nanoparticle layers were to be deposited, the substrates were left to cool to room temperature before subsequent coating. After all interlayers were complete, silver electrodes were evaporated in the usual way.

For testing *n*-PCBM nanoparticles as electron extraction layers, the interlayer was deposited as above onto an FTO-glass substrate, with the intention that a polymer blend BHJ could be deposited on top as discussed in the next section.

4.2 Results and discussion

One issue encountered in synthesizing the nanoparticles as above was the difficulty in separating spiro-OMeTAD nanoparticles from the aqueous surfactant solution. The density of spiro-OMeTAD has been measured as $1.02 \pm 0.03 \mathrm{g/cm^3}$ — almost the same as water. [46] After centrifuging for 18 hours the supernatant (that is, the liquid remaining above the solid material forced to the end of the centrifuge tubes) was still visibly dark red in colour, indicating the presence of doped spiro-OMeTAD. In an effort to increase the yield, water miscible solvents such as methanol and isopropanol were added just prior to centrifuging to lower the overall density of the carrier liquid. Unfortunately each attempt was unsuccessful — the presence of the additional solvents during centrifuging resulted in the nanoparticle material turning a green-grey colour. The nature of this change in colour and the process causing it has not been investigated but is perhaps indicative of the breakdown of spiro-OMeTAD molecules. Dispersions of PCBM did not share this problem as its higher density ($1.5 \mathrm{g/cm^3}$, [66]) allowed effective separation.

Initial experiments to incorporate doped layers of spiro-OMeTAD into DSSCs have shown promising results. Device performance characteristics are shown in figure 4.3. Figure 4.4 compares the current density-voltage plots for devices with a *p*-spiro-OMeTAD nanoparticle layer and the controls averaged over all devices. Mean values for short-circuit current are over $1 \mathrm{mAcm^{-2}}$ higher, resulting in higher efficiencies overall, though a voltage drop of around 350mV is seen on average and fill factors are lower. The fact that devices with the interfacial layer have lower shunt resistance appears to

suggest that although hole extraction may have been improved, the interface is not highly selective in the charge it lets through. Given the assumed band structure should prevent electrons being extracted at the cathode (see figure 4.1), this is suggestive of either there being a morphological or fabrication issue with the interface, or the band structure differing from expectation — it is postulated that migration of dopant ions, either from the *p*-type nanoparticles to the bulk spiro-OMeTAD or the additives from the bulk migrating to the nanoparticles, may account for any unexpected electronic properties at the junction causing the increased dark currents observed. Also shown in figure 4.3 are results for DSSCs with *n*-PCBM between the bulk HTM and silver, to see if the doping level was sufficiently high to allow electrons in the fullerene LUMO to recombine directly with holes in the spiro-OMeTAD HOMO. The cells performed slightly worse than the controls, though there is a chance that this might have been better had a lower work function metal such as aluminium been used as the electrode in place of silver to improve electron injection into the *n*-PCBM from the external circuit.

In addition to standard devices, diodes were made to investigate the spiro-OMeTAD/nanoparticle/silver junction. Using the protocol outlined in chapter 3 mesoporous Al_2O_3 was coated onto FTO glass substrates to allow coating with spiro-OMeTAD. The doped nanoparticles and silver electrodes were deposited as above, and current density-voltage measurements were made on completed diodes under no illumination (figure 4.5). Current densities are higher for bulk spiro-OMeTAD/*p*-type spiro-OMeTAD nanoparticle/silver junctions below 1V (black triangles) than bulk spiro-OMeTAD/silver junctions, showing that hole collection is more efficient in the normal device

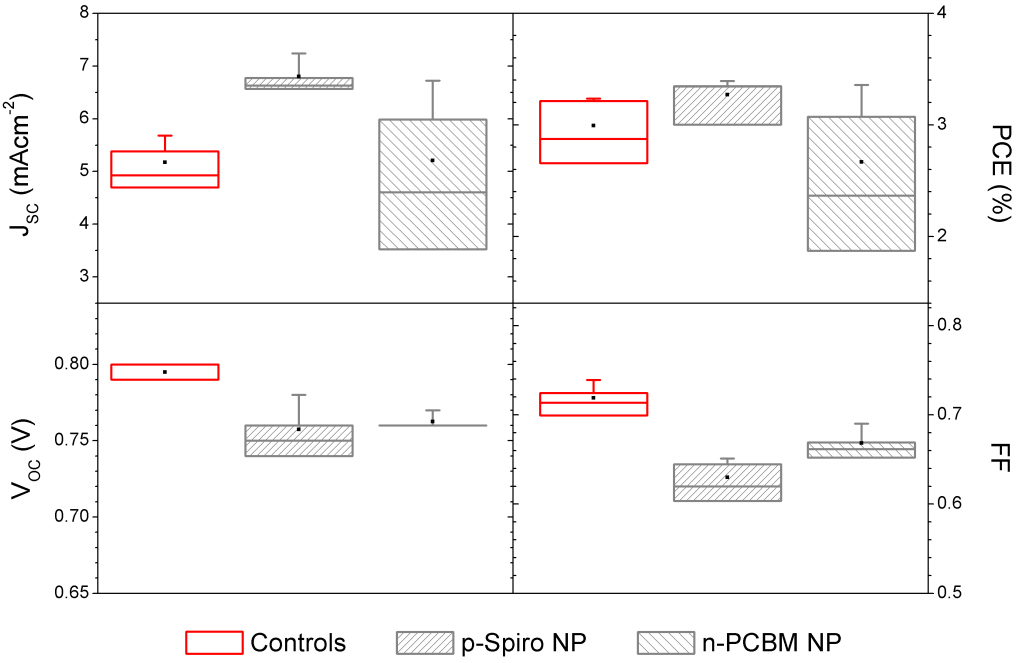

Figure 4.3: Performance parameters of DSSCs with spiro-OMeTAD and PCBM nanoparticle interfacial layers added between bulk spiro-OMeTAD and silver contacts. Extracted from current voltage measurements under simulated solar illumination. Box plots showing outlier, upper and lower quartile and median values for short circuit current density J_{SC}, open circuit voltage V_{OC}, power conversion efficiency PCE and fill factor FF. Mean values indicated by black squares. Data set includes 4 devices of each type.

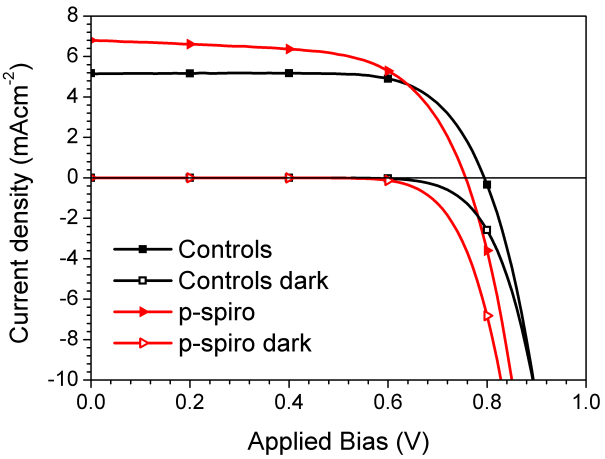

Figure 4.4: Averaged current density-voltage plots for DSSCs with (red triangles) and without (black squares) *p*-spiro-OMeTAD interfacial layer, extracted under simulated AM1.5 illumination (solid symbols) and in the dark (open symbols). Data set includes 4 devices of each type.

operating regime.

As an aside an *n*-*p* junction in the form of a layer of doped spiro-OMeTAD nanoparticles followed by PCBM nanoparticles was cast on top of standard DSSCs utilising D102 dye to see if they too would improve charge extraction — a junction of this type would have potential for use as a recombination interconnect in tandem devices. They did not compare favourably to the control devices as can be seen in figure 4.6 with significant reductions in open circuit voltage, fill factor and efficiency.

UV-IR absorption spectra for films of nanoparticles on glass are shown in figures 4.7 and 4.8. The films are strongly scattering, indicated by the slow tail off in absorbance with increasing wavelength. This masks the characteristic peaks that indicate doping that appear at around 500nm and 700nm in the case of oxidised spiro-OMeTAD, and at 1000-1200nm in C_{60} derivatives

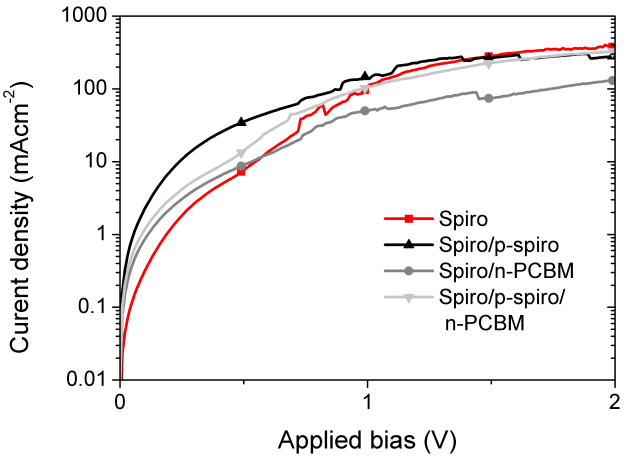

Figure 4.5: Averaged current density-voltage characteristics of doped nanoparticle diodes in the dark: nanoparticle layers/bilayers deposited on a film of spiro-OMeTAD on FTO with an Al_2O_3 scaffold as described in the text. Data set includes 10 measurements on bulk spiro-OMeTAD diodes, and 11 measurements on each of the other diodes measured.

such as PCBM. [28, 67]

When re-dispersing the nanoparticles in isopropanol, a rinsing step (i.e. centrifuging the dispersion in isopropanol and re-dispersing a second time) was deliberately not included to remove residual surfactant in the hope that its presence would decrease nanoparticle solubility in organic solvents as reported by Snaith et al. [68] Unfortunately this was not the case, and films of PCBM nanoparticles would dissolve instantly in chlorobenzene. In order to test the suitability of such a film for use as an electron extraction layer in a P3HT:PCBM bulk heterojunction solar cell (the photoactive material being processed from chlorobenzene), a protective layer of appropriate electronic properties was needed to stop the nanoparticles being washed away during active layer deposition. A 50nm layer of TiO_2 was used to achieve

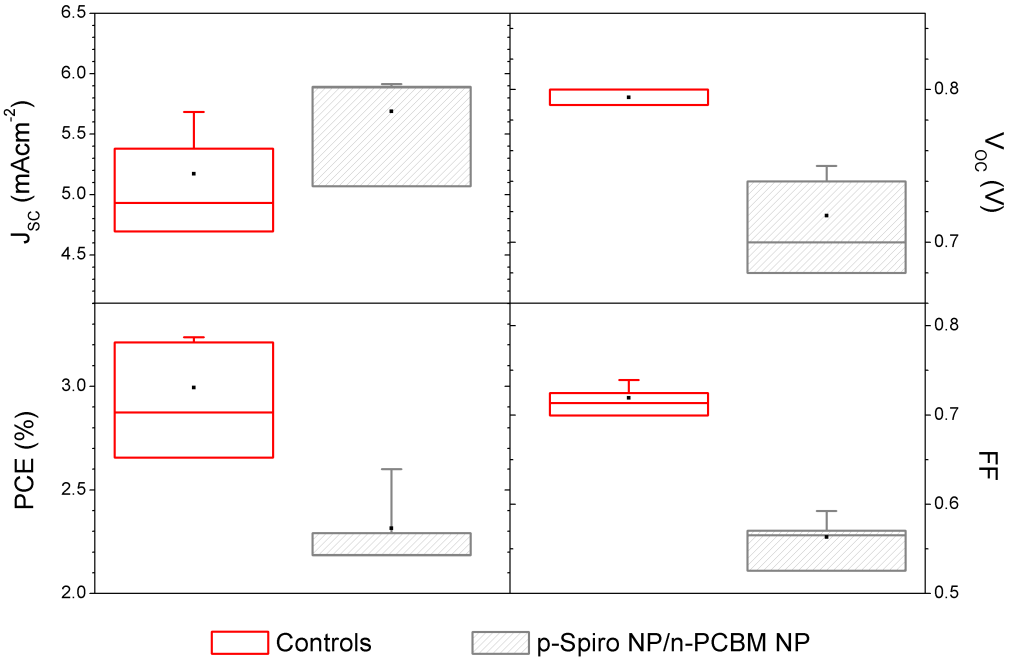

Figure 4.6: Performance of D102-sensitized DSSCs with *p*-spiro-OMeTAD/ *n*-PCBM diode coated on top as described in the text, extracted from current voltage measurements under simulated solar illumination. Box plots showing maximum, minimum, upper and lower quartile and median values for short circuit current density J_{SC}, open circuit voltage V_{OC}, power conversion efficiency PCE and fill factor FF. Mean values indicated by black squares. Data set includes 4 devices of each type.

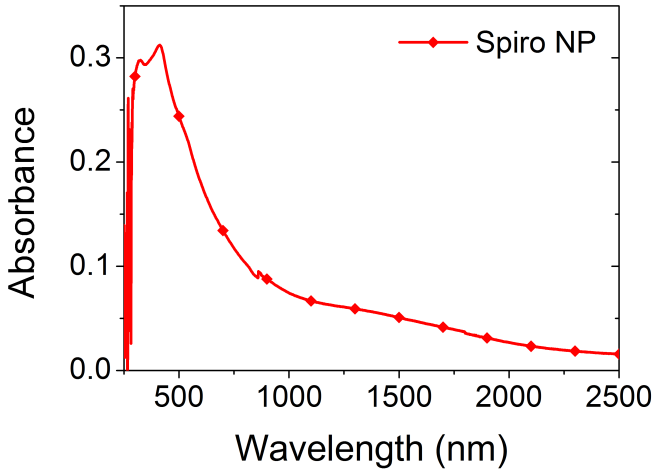

Figure 4.7: Spiro-OMeTAD nanoparticle absorption spectrum.

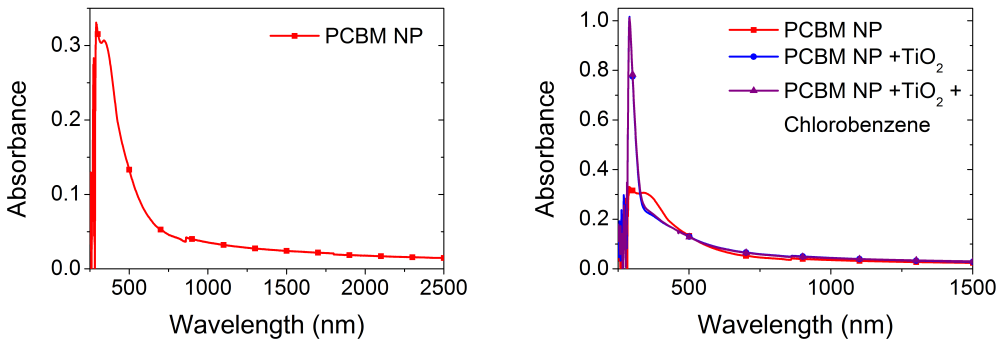

(a) (b)

Figure 4.8: PCBM nanoparticle dispersion absorption spectra. 4.8a) nanoparticles coated on glass. 4.8b nanoparticles on glass (red line), coated with a layer of TiO_2 (blue line) and coated with TiO_2 followed by neat chlorobenzene (purple line).

this — a titania sol was created by mixing titanium isopropoxide, ethanol and hydrochloric acid as fully described in chapter 5, and was spin coated at 1500RPM for 45s and annealed at 150°C for 10 minutes.

Figure 4.8 shows the spectra of the same film of PCBM nanoparticles on glass covered with protective TiO_2 both before and after spin coating neat chlorobenzene on top (blue and purple lines respectively). The data are virtually indistinguishable, indicating that chlorobenzene cannot permeate the TiO_2 and remove material from the nanoparticle layer. P3HT:PCBM bulk heterojunction devices were fabricated on top of such doped PCBM nanoparticle/TiO_2 bilayers on FTO electrodes, and on top of TiO_2 only (processed in the same way) on FTO. Sadly these results were poor, as demonstrated by the example current density-voltage curves shown in figure 4.9. The low currents and poor rectification, coupled with little change to open circuit voltage are symptomatic of a very large series resistance being present, most likely due to the *n*-PCBM/TiO_2 bilayer being highly resistive and/or its components making poor electronic contact to each other. This might arise if the *n*-doping of the PCBM (band gap 2.5eV, [69]) was too low, such that Fermi level alignment when in contact with TiO_2 (band gap 3.25eV, [70]) caused its LUMO level to lie higher in energy than the conduction band of the TiO_2. It is noted that no characteristic peak in the absorption spectra for supposedly doped PCBM is seen, though whether it is present and masked by scattering effects is unclear.

SEM images were taken to examine the morphology of films of nanoparticles spin cast on glass (figures 4.10 and 4.11). Again, films of both nanoparticle types are discontinuous as coated, and as with the TMDCs it is possible

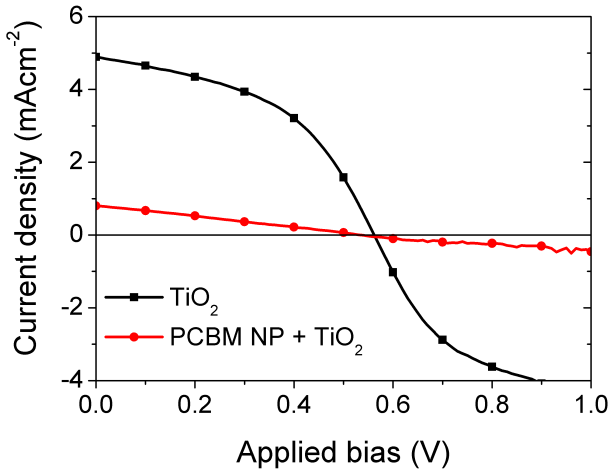

Figure 4.9: Example current density-voltage characteristics extracted under simulated AM 1.5 illumination for P3HT:PCBM BHJ solar cells with and without a PCBM nanoparticle interfacial layer between FTO anode and TiO_2 hole blocking layer.

that the full benefits of the interfacial layers is being lost thanks to incomplete coverage of the area over which charge is being extracted.

Attempts were made to determine the conductivity of doped nanoparticles cast on glass using the four terminal technique described in chapter 2, though unfortunately the discontinuity of the films made the measurement impossible.

After casting and heating, *p*-doped spiro-OMeTAD forms a mesoporous network of nanoparticles with dimensions on the order of 100nm. In contrast, *n*-PCBM structures appear less porous and are formed of nanoparticles around 50nm in diameter. Other, larger structures are also seen.

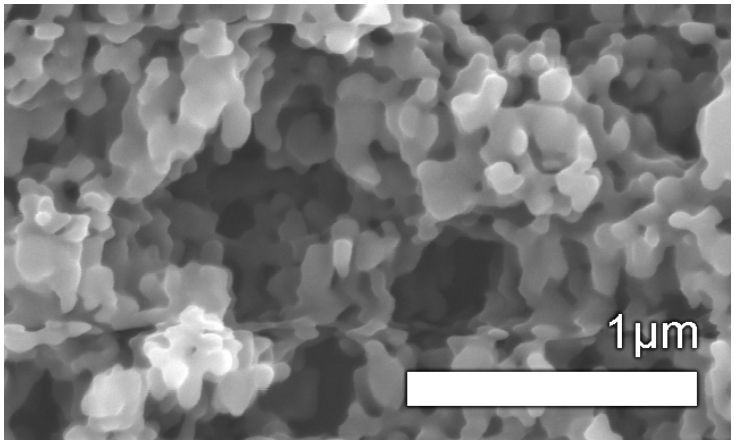

(a)

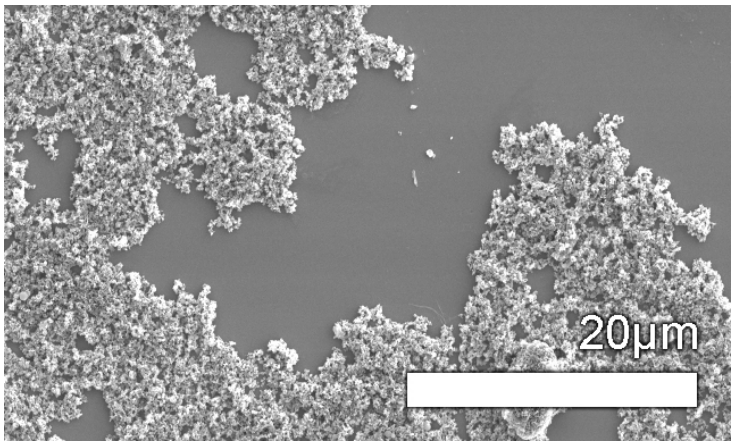

(b)

Figure 4.10: SEM images of doped spiro-OMeTAD nanoparticle film deposited by spin coating as described in the text.

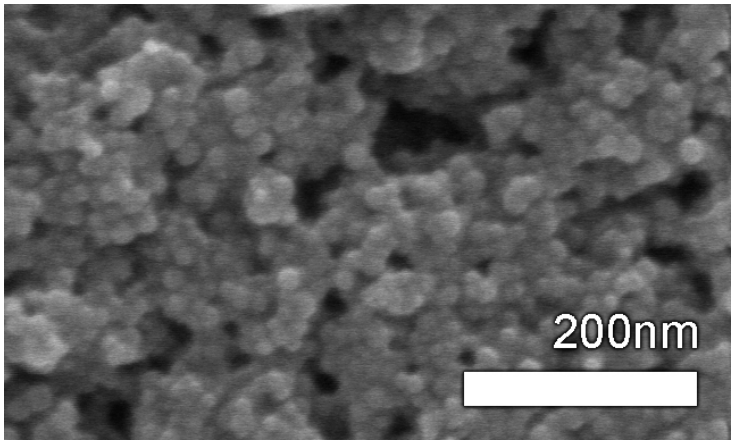

(a)

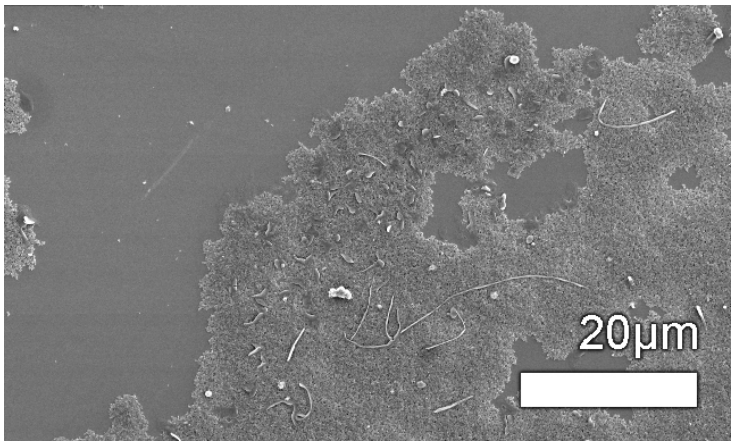

(b)

Figure 4.11: SEM images of doped PCBM nanoparticle film deposited by spin coating as described in the text.

4.3 Conclusion

Again electronic modification of the spiro-OMeTAD/silver junction has led to improved device performance. By adding a thin layer of heavily *p*-type doped hole transporter at the interface, devices produce higher currents and thus efficiencies. Critically, though this architecture is well known for inorganic photovoltaic technologies, implementation in DSSCs required the relatively novel technique of synthesizing of nanoparticle dispersions to allow the use of orthogonal solvents, which has been successfully demonstrated here. Deposition of such interlayers requires optimisation to get continuous and uniform film formation, and it is hoped that this may solve issues with decreased shunt resistance seen in devices and allow further improvement to efficiency to be made.

To the same end *n*-type doped PCBM dispersions were synthesized for use as electron extraction layers in polymer blend BHJ cells, though processing issues meant their success was limited. Presence of residual surfactant did not make films solvent resistant, and doping levels were not sufficient to allow TiO_2 to be used as an intermediate protection layer and maintain good electron extraction properties. Further investigation into appropriate reducing agents and protective interlayers would be necessary to achieve functioning electron extraction layers of this format.

Chapter 5

Tandem devices

Whilst there has been significant research into creating tandem liquid electrolyte dye-sensitized solar cells, mainly focussed on creating p-type photoanodes, comparatively little work has been done on their solid-state counterparts. [71,72] This is due in part to the inability to process multiple sub-cells on top of one another as outlined in chapter 1. Following the successful demonstration of the novel charge extraction interfaces reported in chapters 3 and 4, they were assessed for their suitability as series interconnect components for use in hybrid tandem devices using solid-state DSSC and BHJ sub-cells, and compared against a well-known recombination layer format from literature.

5.1 Sub-cells

In our device configuration, sunlight enters through the FTO-coated glass substrate. Since a low band gap absorber can absorb the high energy pho-

tons (resulting in a portion of their kinetic energy being lost through thermalisation as the excited electrons relax to the absorber's LUMO level), it is important that light reaches the high band gap absorber in a tandem solar cell first. Thus the first sub-cell (the DSSC in this case) can filter out photons with energies higher than its band gap. Devices sensitized with the dye D102 as used throughout the preceding experiments absorb strongly over a large segment of the solar spectrum, with a broad peak in absorbance roughly centred around 500nm. A more appropriate indoline dye for use in the sub cell is D131 which has stronger absorption towards the blue, i.e. higher energy end of the visible spectrum and weaker absorption in the red. Absorbance spectra for DSSCs using D102 and D131 are shown in figure 5.1 for comparison (the cells have no silver electrodes, but are otherwise complete). Also shown are the spectra for both P3HT:[60]PCBM and PCPDTBT:[70]PCBM bulk heterojunctions (in this case only showing absorbance of the active layer, not a complete device). The low band gap photoactive polymer PCPDTBT is a good candidate for efficient BHJ solar cells and has achieved good power conversion efficiency when used with the C_{70} form of PCBM as an electron acceptor. [39, 73] It absorbs out into the near infrared, with little spectral overlap with a D131 DSSC, thus these two systems were chosen for tandem devices.

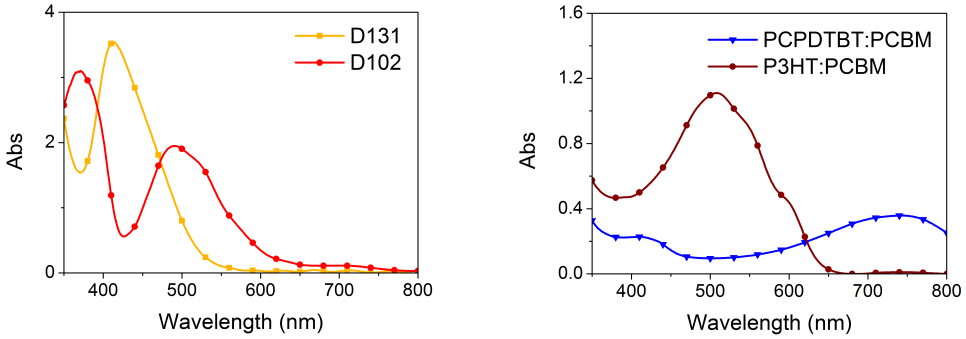

(a) (b)

Figure 5.1: DSSC and BHJ absorption spectra comparison. 5.1a) DSSC devices without silver electrodes using the indoline dyes D102 and D131 (referenced to air), fabricated as described in section 2.1 (D131 sensitization followed same protocol as D102). 5.1b) Spectra of polymers P3HT and PCPDTBT each blended with PCBM according to section 2.1 coated on glass (referenced to similar glass substrate).

5.2 Recombination interfaces

As previously mentioned, the key qualities a series interconnect must possess are ohmic contacts with each sub-cell, an appropriate electronic environment for electrons from one sub-cell to recombine with holes from the other, and high optical transmission over the spectral range in which the rear sub-cell is active. In the field of tandem organic photovoltaics a number of different approaches have been reported including using thin layers of metal, transparent conductive oxides, carbon nanotubes and other organic and inorganic semiconductors, and various combinations thereof. [30, 74–77] Many require deposition under vacuum (e.g. thermal evaporation or sputter coating) though there are some that can be processed from solution, for example bi-layers consisting of either TiO_2 or ZnO as the electron collection component and PEDOT:PSS for hole collection — for these particular

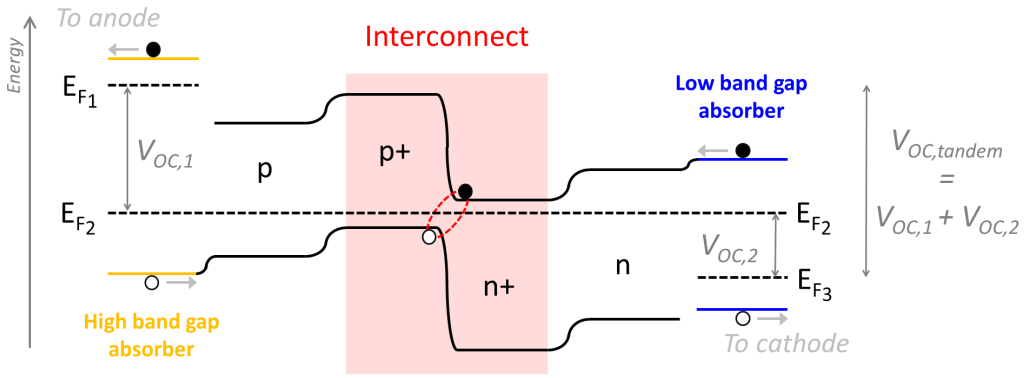

Figure 5.2: Illustrative energy bands for a generic tandem DSSC, showing two absorber materials, the high band gap sub-cell hole transporter (p), the low band gap sub-cell electron transporter (n), the series interconnect and the positions of the quasi Fermi levels (E_F). A tunnel junction across which electrons and holes can recombine forms the interconnect — this may consist of a heavily *p*-type doped hole transporter/heavily *n*-type electron transporter interface as shown above, or use alternative materials such that the band profile for electrons and holes is similar. For a current matched device, the open circuit voltage is equal to the sum of those for the sub-cells. Horizontal axis represents distance.

examples the interlayer is thought to behave as a metallic contact to each sub-cell. [78] Having shown in chapter 3 that TMDC layers are effective hole extraction layers, they were compared against PEDOT:PSS in bi-layers with TiO_2. Tandem solar cells were made in the following format: DSSC sub-cell/TMDC interlayer/TiO_2/BHJ sub-cell.

Conversely, traditional inorganic photovoltaics generally achieve a good recombination layer through the use of a highly doped p-n junction as shown in figure 5.2. [79] The hope was that the doped nanoparticle dispersions investigated in chapter 4 could be used to make such a junction, with a p-spiro-OMeTAD/n-PCBM bi-layer between DSSC and BHJ sub-cells, offering a new kind of interconnect in the context of organic photovoltaics. Unfortunately as reported previously it was not possible to protect the coated nanoparticles from the solvents from which the BHJ material is cast whilst maintaining functioning devices. Instead a structure similar to that for the TMDC interconnects was used: heavily doped p-spiro-OMeTAD nanoparticles would coat a DSSC sub-cell, followed by a layer of TiO_2 and a BHJ rear sub-cell.

It is noted that although both films of TMDC and of cast spiro-OMeTAD and PCBM doped nanoparticles absorb in the visible spectrum, they do so weakly, and mostly towards the high energy region, peaking below 500nm (as recapped in figure 5.3). As the recombination layer need only let lower energy photons through to the rear sub-cell, both the TMDCs and nanoparticles should be optically satisfactory for use as tandem interconnects. The possible shortcomings of TMDC and doped nanoparticles in terms of film formation have also been discussed, but for the purposes of use in a series interconnect a

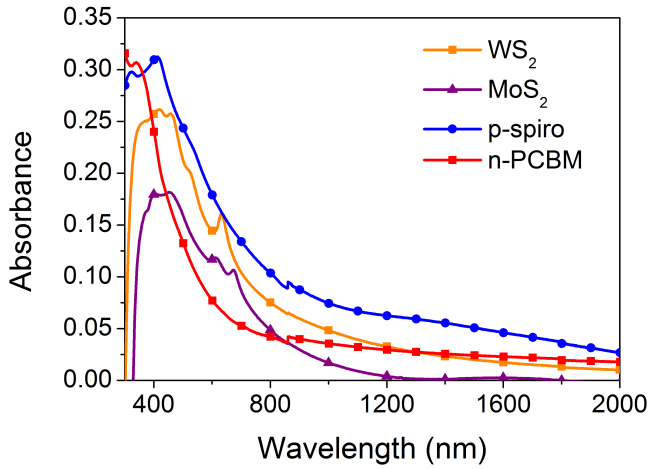

Figure 5.3: Summary of TMDC and doped nanoparticle absorbance characteristics reported in chapters 3 and 4.

discontinuous layer should be sufficient to provide ample recombination sites (there should be little direct transfer of electrons from the TiO_2 interlayer component to the bulk spiro-OMeTAD, and little transfer of holes in the opposite direction). [80] It is however important that the TiO_2 component is continuous — if there are gaps in the layer both the photoactive polymer and the electron acceptor phases could contact the bulk spiro-OMeTAD and it is possible unwanted charge transfer between the various components could occur.

If the current produced by the DSSC and BHJ in isolation is not similar, when connected in a series tandem configuration the excess electrons and holes from the high current sub-cell will build up in the interconnect/electrode material at the interface with the low-current sub-cell. This reduces the electric field and thus voltage across the high-current sub-cell which in turn reduces the extracted current. The opposite happens in the low-current sub-

cell until the current through each cell is matched. [81] To maximise the current output for a given pair of sub-cells it is desirable that they produce similar currents in isolation. The current density J and voltage $V(J)$ of the tandem device and sub-cells 1 and 2 under operation are governed by equations 5.1 and 5.2 respectively:

$$J_{tandem} = J_1 = J_2, \tag{5.1}$$

$$V_{tandem}(J_{tandem}) = V_1(J_1) + V_2(J_2), \tag{5.2}$$

when equation 5.1 is satisfied. [81] Therefore at open circuit ($J_{tandem} = 0$) the voltage across the tandem device is equal to the sum of the open circuit voltages of the sub-cells in isolation.

5.3 Experimental details

DSSC preparation follows section 2.1, with the exception that the indoline dye D131 was used (dissolved in acetonitrile:tert-butanol mix, 1:1 by volume, at 0.1mg/ml) and that the substrates coated with mesoporous TiO_2 were only placed in a dye bath for 5 minutes as explained below. A portion of completed DSSCs were set aside for silver electrode deposition to act as sub-cell controls. Similarly, PCPDTBT:[70]PCBM control cells were prepared according to section 2.1.

The series interconnects were processed directly onto D131 DSSCs without silver electrodes. Firstly the hole collecting component was coated; either PEDOT:PSS (Clevios) spin coated at 2000RPM for 45s then dried at 140°C

for 10 minutes, or a layer of TMDC or doped organic nanoparticles deposited as described in chapters 3 and 4 respectively. Following the chosen hole collecting layer, a compact layer of TiO_2 to collect electrons from the BHJ sub-cell was added. Titatium isopropoxide was added to anhydrous ethanol (both Sigma Aldrich) under vigorous stirring in a ratio of 1:6.86 by volume. To this an equal volume of 28mM hydrochloric acid in ethanol was added drop-wise, and the resulting TiO_2 nanoparticle sol was passed through a 22μm filter. This was spin coated on top of the hole collecting component at 1500RPM for 45s, and heated to 150°C to dry the film. The creation of TiO_2 films in this way has been used as an alternative to the spray pyrolysis route for use as the hole blocking compact layer in single junction DSSCs with very similar device performance, so there was every hope that this should work well for tandem interlayers as well. [82]

PCPDTBT:[70]PCBM devices were processed on top of the interlayers and silver electrodes evaporated using the standard protocol. In section 2.1 stress is given to the practice of removing FTO from glass directly beneath the point at which connection pins from external testing apparatus contact the silver cathode to reduce the potential for short circuits. By the same token, care must be taken when testing tandem devices that these pins are not able to pierce through the BHJ sub-cell and contact the interlayer or DSSC component. Before the evaporation of electrodes, all material lying above the regions where FTO had been etched away was removed mechanically, attempting to leave a little overlap for each successive layer (see figure 5.4).

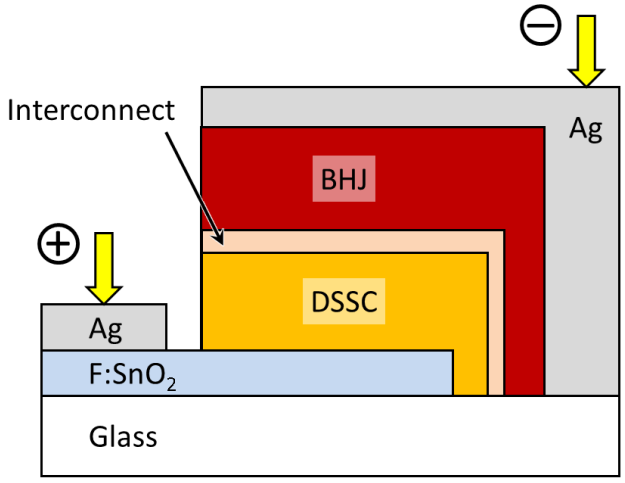

Figure 5.4: Tandem cell cross section schematic showing removal of material below cathode to avoid shorting paths should the contact pin pierce through the silver (not to scale). Light enters the device through the glass side.

5.4 Results and discussion

Tandem solar cells employing D131 solid-state DSSC front and PCPDTBT:[70]PCBM bulk heterojunction rear sub-cells with several different series interconnects were fabricated. Figure 5.5 shows current density-voltage characteristics averaged over all samples for the sub-cells in isolation and for tandem devices using one of the more common interlayers described in literature, namely hole collecting PEDOT:PSS followed by TiO_2 to provide a benchmark against which to compare the new materials. The bulk heterojunction cells for testing in isolation were processed in an identical way to those included in tandem devices, but on top of a substrate of FTO coated glass and spray coated compact TiO_2. All DSSC components were only dyed for 5 minutes to sensitize a smaller fraction of the TiO_2 than usual. This reduced the current output to match it roughly to that of the PCPDTBT:[70]

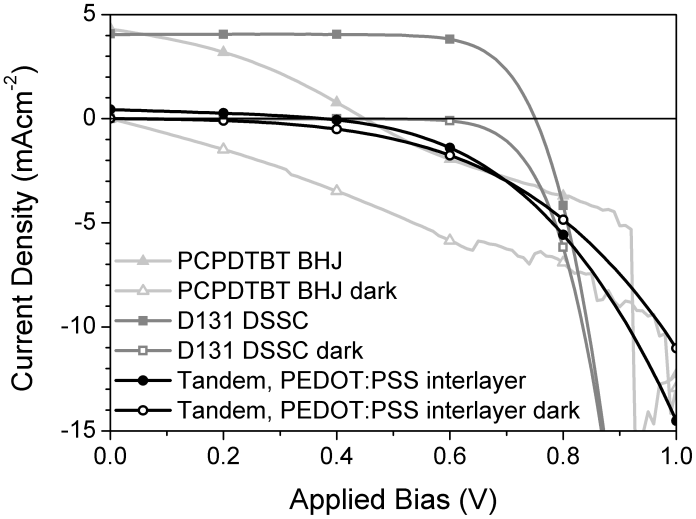

Figure 5.5: Averaged current density-voltage curves for tandem cells using PEDOT:PSS/TiO_2 interconnect (black circles) and for D131 DSSC (dark grey squares) and PCPDTBT BHJ (light grey triangles) sub-cells. Curves extracted under simulated AM 1.5 solar illumination (solid symbols) and in the dark (open symbols). Data set includes 6 polymer BHJ control cells, and 8 devices of each other type.

PCBM sub-cells. Figure 5.5 shows that the currents are similar on average at short-circuit.

Whilst it was not expected that tandem devices should outperform single junction solar cells in terms of efficiency on the first attempt, a working interconnect should yield higher open-circuit voltage than either sub-cell in isolation. The fact that tandem V_{OC} is on average lower than for either sub-cell raises questions as to the functionality of the recombination layer. It is also worrying that the current density at short circuit is significantly lower than corresponding values for the sub-cells. Similarly, comparison to devices in which PEDOT:PSS is replaced with doped spiro-OMeTAD nanoparticles (figure 5.6) shows the same issues (box plots of V_{OC} for these two tandem

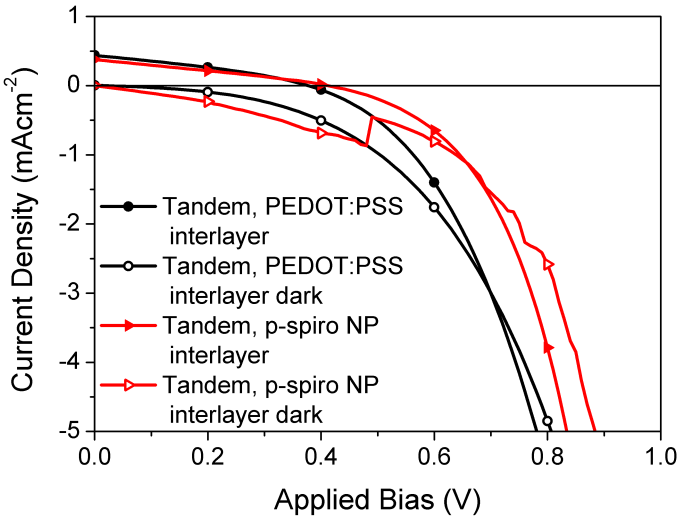

Figure 5.6: Averaged current density-voltage curves for tandem cells using PEDOT:PSS/TiO_2 (black circles) and doped spiro-OMeTAD nanoparticle/TiO_2 interconnects (red triangles). Curves extracted under simulated AM 1.5 solar illumination (solid symbols) and in the dark (open symbols). Data set includes 8 devices of each type.

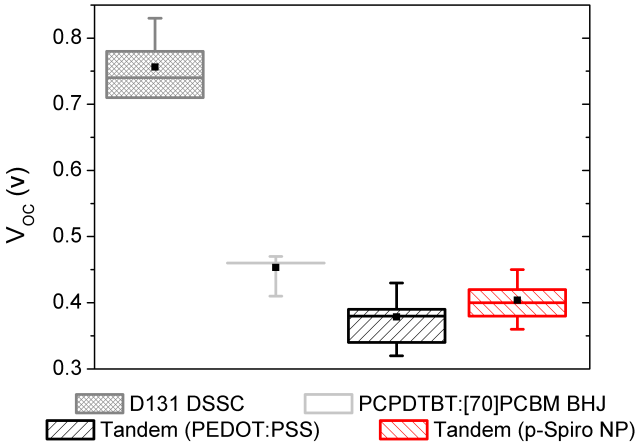

Figure 5.7: Open-circuit voltages of tandem solar cells employing PEDOT:PSS/TiO_2 and doped spiro-OMeTAD nanoparticle/TiO_2 interconnects, and of their sub-cells extracted under AM1.5 simulated solar illumination. Box plots show median, upper and lower quartile, and maximum and minimum values. Black squares indicate mean value. Data set includes 6 BHJ control cells, and 8 devices of each other type.

architectures and their sub-cells can be found in figure 5.7). The dark currents for the tandem devices have a lower magnitude than the BHJ controls, which at least indicates that the overriding problem is not one of shorting directly between the electrodes. Preliminary data also suggested the same problem with TMDC components.

One possibility is that the VB/HOMO in the hole extraction layer and the CB for the TiO_2 interlayer component simply lie too far apart in energy, preventing charge carriers tunnelling across the interface and recombining — the absence of voltage addition in tandem devices implies space charge build up on either side of the recombination junction. [83]. However, given that PEDOT:PSS/TiO_2 interlayers have been successfully demonstrated by others for all-polymer BHJ tandem devices (for example, [78, 84]), it is somewhat

surprising that results should be so poor when used with a DSSC sub-cell.

Following Hadipour et al. analysis of the individual sub-cell current responses can provide the current-voltage curve of the tandem device in the case of a perfect interlayer and no charge build-up. [81] Using equations 5.1 and 5.2, the voltage for each sub-cell at a number of different currents can be extracted (figure 5.8, blue lines) — the sum of the voltages gives the bias that needs to be applied to the ideal tandem cell to generate the chosen current. Before this can be done, the response of the BHJ control devices must be adjusted to account for the part of the solar spectrum filtered out by the D131 top cell. The modified photocurrent (the measured current response under illumination minus the response in the dark) was calculated using the adjusted radiation spectrum that would reach the PCPDTBT:PCBM sub-cell and added to the previously measured dark current to obtain the curve shown in figure 5.8. The current density-voltage characteristics for a tandem D131 DSSC and PCPDTBT:[70]PCBM cell with a perfect interlayer is shown around open circuit in figure 5.9, and reinforces the assumption that the interconnect is to blame for poor performance (unfortunately this curve cannot be extended to short circuit as control device data was not collected in reverse bias).

To ascertain whether the problem was due to the fabrication process as opposed to the material components, SEM images were taken at various stages of tandem cell fabrication to observe the morphology of the successive layers making up the interconnect as they are deposited. Figure 5.10a shows the DSSC sub-cells spiro-OMeTAD surface before any interlayer processing has been undertaken. Droplet-like structures up to several millime-

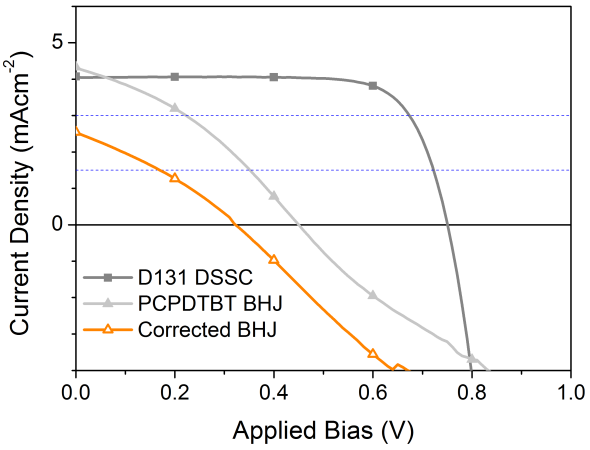

Figure 5.8: Modelling ideal tandem cell performance using averaged sub-cell characteristics. For a given current (blue dashed lines) the applied bias to each sub-cell is added together to give the voltage required to generate the same current in a tandem device with a perfect interconnect. The corrected curve for the BHJ sub-cell was obtained by factoring in the effect of light filtered by the D131 sub-cell as described in the text. Data set includes 8 DSSC control cells and 6 polymer BHJ cells.

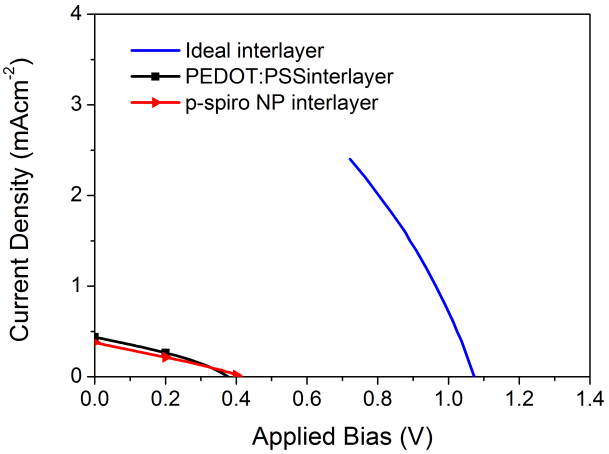

Figure 5.9: Simulated current density-voltage curve at open circuit for tandem devices with perfect interconnects, calculated from the averaged responses of individual sub-cells in isolation (subject to appropriate light filtering corrections as discussed in the text) shown in figure 5.8. Comparison to actual fabricated tandem devices is shown (data set includes 8 tandem devices for each interlayer).

tres in length are clearly seen, caused by the hole transporter solution dewetting to some extent during casting. The root of this problem is as yet unknown and only appears in certain batches of spiro-OMeTAD material, but has little effect on device performance for single junction DSSCs. Following spray deposition of PEDOT:PSS, the undulations can still be seen (figure 5.10b). It is after the deposition of TiO_2 nanoparticles that the effect of the "droplets" of spiro becomes clear. Figure 5.11 shows a nominally complete PEDOT:PSS/TiO_2 interconnect at a range of magnifications. The TiO_2 film quality is mostly good (though appears to be porous) where the underlying spiro-OMeTAD film is flat, but significant cracks can be seen in many sites above the locations of hole transporter "droplets". When the solution of polymer blend is cast, it is therefore able to contact the surface

of the PEDOT:PSS directly through the cracks, and potentially through the pores in the film. PEDOT:PSS (and quite possibly *p*-spiro-OMeTAD nanoparticles and WS_2/MoS_2) can effectively extract holes from PCPDTBT as well as spiro-OMeTAD. [39] If the photoactive polymer is also permitted to contact the PEDOT:PSS, holes from *both* sub-cells may accumulate at the interconnect, to the detriment of device current density and open-circuit voltage.

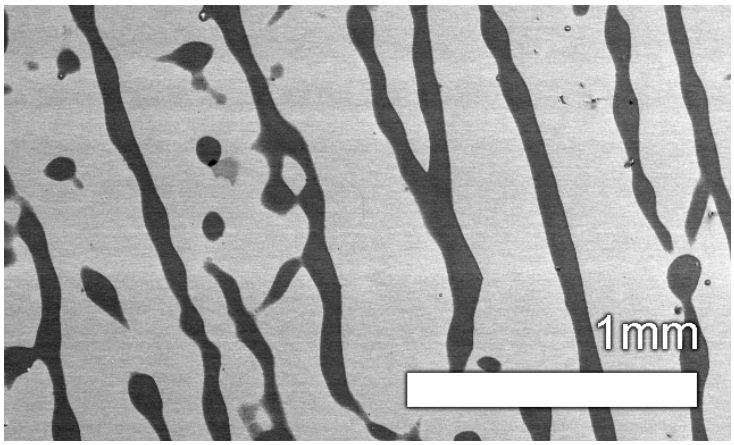

(a)

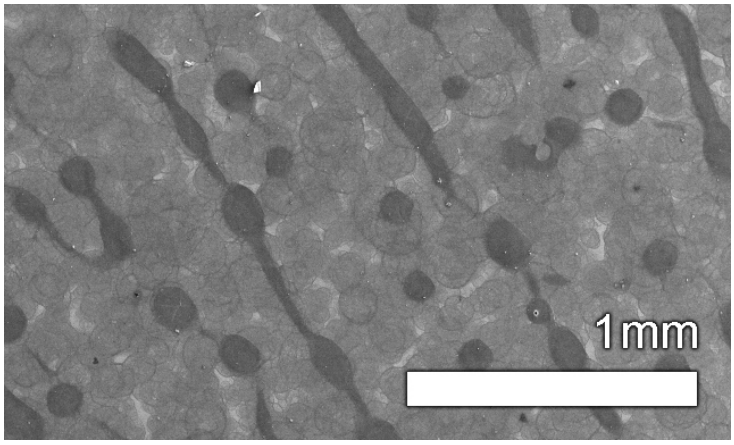

(b)

Figure 5.10: SEM image of spiro-OMeTAD surface of DSSC sub-cell before interconnect deposition (5.10a), and of PEDOT:PSS on DSSC sub-cell deposited via aerosol spray (5.10b).

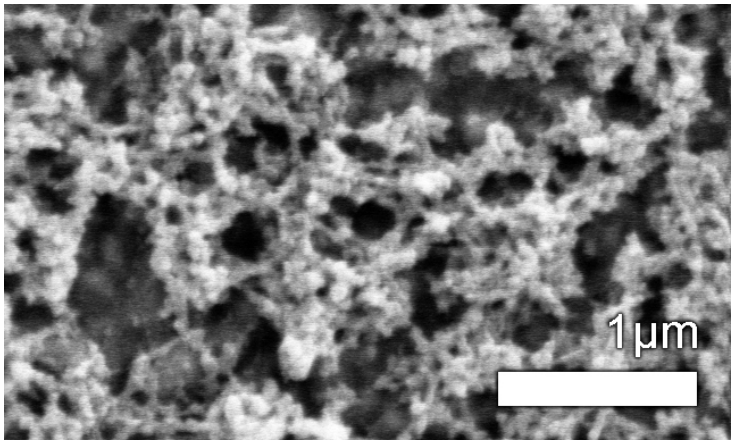

(a)

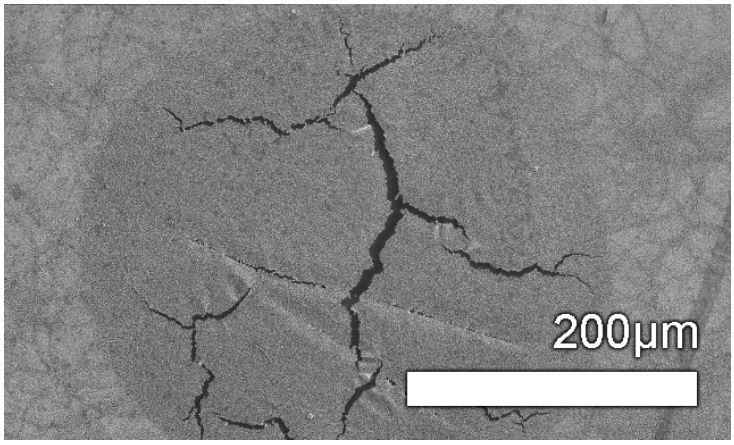

(b)

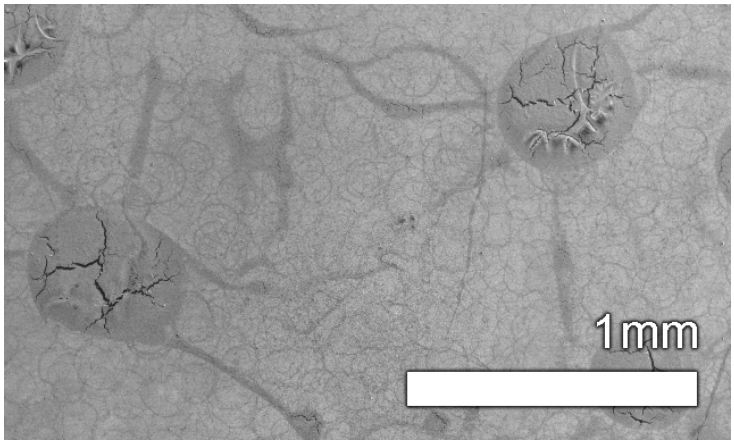

(c)

Figure 5.11: SEM images of TiO_2 nanoparticle film deposited by spin casting on top of PEDOT:PSS-coated DSSC sub-cell as described in the text.

5.5 Conclusion

To summarise, tandem devices have been made via an entirely solution-processed route, utilising a DSSC front sub-cell to capture higher energy photons and a low band gap polymer bulk heterojunction sub-cell to harvest radiation over much of the rest of the solar spectrum. Different series interconnects have been investigated, including the well-known PEDOT:PSS/TiO_2 architecture, and those using the novel transition metal dichalcogenide or doped organic semiconductor nanoparticle hole extraction layers reported in earlier chapters in conjunction with the same TiO_2 sol component. Though these cells did function, in that they showed rectification and some photocurrent generation, their performance was poor. Most importantly the open circuit voltage of devices utilising any of the aforementioned interconnects was less than that of either of the sub-cells in isolation. Knowing that the key components function well by themselves suggests that the issue may be one of fabrication. Scanning electron microscopy seems to indicate that surface roughness in the DSSC hole transporter film may be to blame. It is possible that more success would be had if an alternative hole transporter material with better film forming properties on dyed TiO_2 and low absorbance over the solar spectrum could be found. It is worth noting that previous reports on OPV tandem devices have been processed on ITO coated glass, which has a lower surface roughness than glass coated with FTO — this may be more important in tandem solid state-DSSCs than single junction devices, given that their architecture requires the use of multiple thin layer components.

Chapter 6

Large area hole transporter deposition in mini-modules

This chapter takes a departure from series interconnects designed for tandem DSSCs of the format described thus far to look at modular DSSC designs for large area processing. In it the viability of large area processing for solid-state dye-sensitized solar cells is demonstrated for the first time by fabricating 'mini-modules' comprising two 4cm^2 photoactive regions connected in series, using the technique of doctor blade coating to deposit the hole-transporter material. For the optimised protocol only 25% of the power conversion efficiency is lost when compared to standard test devices which have only 0.12cm^2 active area. By estimating pore-filling fractions using reflectance spectroscopy, it is shown that device performance is linked to changes in the volume of the mesoporous TiO_2 photoanode infiltrated with hole-transporter as deposition temperature is varied.

Part of what makes organic photovoltaic technologies attractive is the

fact that typically components may be processed from solution, making them compatible with high through-put manufacturing techniques. [85–87] With an aim for the commercialisation of these technologies it is important to prove that their fabrication can be scaled up to the device sizes required for practical power generation. Most DSSC components are already processed using scalable methods, with the exception of hole transport/dye regeneration media. Electrolyte DSSCs are intrinsically not ideal for large area manufacturing — although they can boast higher power conversion efficiencies than their solid-state counterparts, they require that both the sensitized photoanode and the cathode be assembled and sealed before filling with an electrolyte. This combined with the very careful sealing required to prevent the corrosive liquid leaking during long term operation makes scaling up more involved and challenging than the simple process of coating each component monolithically in a solid-state DSSC. Presently, the laboratory-scale method for depositing the hole-transporter is via spin coating from solution. [43] Because this method requires the substrate to be rotated at high speeds, it is impractical for use when scaling-up production from small test devices (typically 1 to 2cm^2 [88]) to production size modules on the order of m^2.

One possible solution is to use the technique of doctor-blade coating (or doctor-blading). This has the additional benefits over spin-coating of producing films of more uniform thickness and the potential for reduced wastage of coating solution. [85] For this specific purpose, the process involves depositing a solution containing the hole transporting material onto the sensitized photoanode and coating it across the top of the porous film by moving a bar or blade (held at a defined height above the substrate) across the active

area. As the bar moves, it pushes a "reservoir" of hole-transporter solution over the photoanode. The solution wets the mesopores below the reservoir through capillary action, and a thin wet film of order 10μm thick is left in the wake of the blade. Upon subsequent solvent evaporation, the hole-transporter concentrates into the pores until the top of the film solidifies (i.e. forms a skin), and no more hole-transporter is available from the reservoir to fill the pores. Further solvent evaporation from within the porous film will leave voids, and a porous dye-sensitized electrode partially filled with hole-transporter. [42–45] From previous studies on spin-coating it is apparent that the hole-transporter approximately uniformly fills the pores from the top of the film to the bottom, but not completely. [42, 44] The ratio of the volume of hole transporter occupying the pores after the carrier solvent has evaporated to the total volume of the porous network is defined as the pore-filling fraction (PFF). Typically for spin-coating, pore-filling fractions of between 60% and 80% can be readily achieved for spiro-OMeTAD. [43, 46] The blade height influences the thickness of hole-transporter left above the photoanode for a given coating solution viscosity, but notably a meniscus behind the bar will ensure that the as-coated wet-film is less thick than the blade height. This has been successfully demonstrated for solid-state DSSCs on small test devices measuring 1.5cm×2cm by Ding et al. [89] Here, this work is extended to process larger area mini-modules, and vary coating temperature to assess its influence on mesopore infiltration with the hole-conductor and module performance. Schematics illustrating the structure of the modules and the process of doctor-blade coating are shown in figure 6.1.

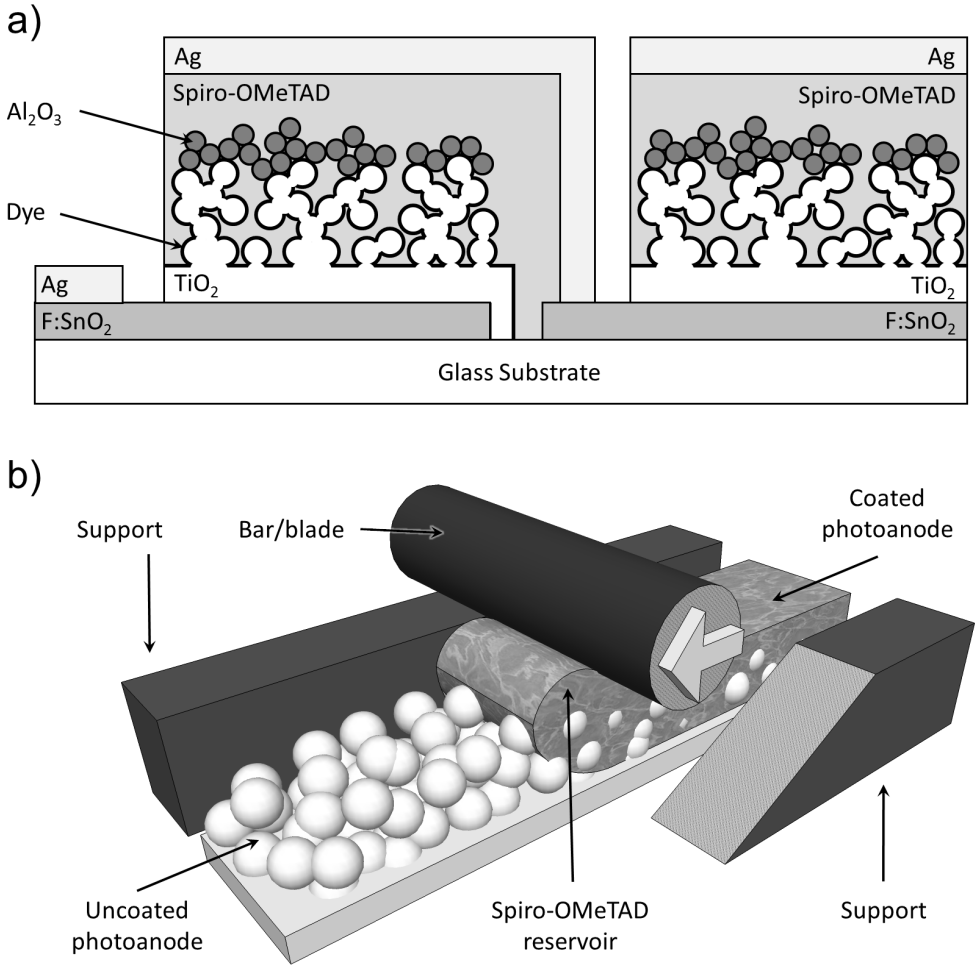

Figure 6.1: a) Schematic showing the cross section of a mini-module. The spiro-OMeTAD capping layer is defined as the material between the top of the mesoporous metal oxides and the bottom of the silver cathode. Al2O3 was added to block possible shorting paths between the silver and TiO_2. Other components in the solar cell are labelled. b) Diagram to illustrate the process of doctor-blading. Spiro-OMeTAD solution is deposited onto the prepared photoanode just in front of a bar or blade. The bar is pushed across the rest of the mesoporous structure held at a defined height by supports either side of the substrate (from right to left in figure above). A reservoir of solution ahead of the bar provides material to wet and fill the mesopores, with the bar leaving a smooth film in its wake.

6.1 Experimental details

Device fabrication: Device manufacture differed from the standard protocol (see section 2.1) in the following ways. The FTO-coated glass used had a sheet resistance of 15Ω/□ (Pilkington) upon which the compact layer of TiO_2 was deposited by aerosol spray pyrolysis of titanium diisopropoxide bis(acetylacetonate) at the higher temperature of 500°C, using air as the carrier gas. The deposition of the TiO_2 mesostructure and subsequent treatment with $TiCl_4$ was carried out as normal, but before the second heating step to 500°C a home-made Al_2O_3 paste (nanoparticles from Alfa Aesar) was doctor bladed onto each substrate. After sensitizing with D102 and rinsing with acetonitrile the photoanodes were heated to the relevant temperature, before the spiro-OMeTAD solution was deposited as described above. The bar used for doctor blading was held at 50μm above the substrate during deposition by scotch tape spacers.

Device characterization: During current-voltage measurements, the length of the active area was defined by black tape acting as an optical mask, but the width of each cell was defined by the overlap of the fluorine-doped tin oxide and silver electrodes. It is noted that this is expected to introduce a slight overestimation in the photocurrent due to edge effects, though by considerably less in this large cell configuration than the 14% increase reported for small area (0.12cm^2) solid-state DSSCs. [40] Characterization also defined the maximum size of the modules — the solar simulator used only provides reasonably uniform illumination over a square area just over 5cm × 5cm in area, thus the longest module dimension was limited to 5cm.

Pore-filling substrate preparation: Mesoporous TiO_2 films were prepared on bare glass in the same way as described in section 2.1, $TiCl_4$ was applied, but no additional Al_2O_3 layer. No dye was applied after the second baking step. Spiro-OMeTAD was deposited as described above at various substrate temperatures.

6.2 Results and discussion

Since the sheet resistance of the fluorine-doped tin oxide anodes on which the devices were made was high ($15\Omega/\square$), resistive losses limited the width of the active area to approximately 1cm, for up to $20mAcm^{-2}$ photocurrent. This poses a problem when making large area devices, but can be circumvented by connecting multiple thin active strips in series in a modular format to reduce current density whilst boosting voltage, as is standard practice for other technologies. [90,91] In order to test doctor blading as a means to deposit hole transporter materials on a better approximation to a full scale commercial device, DSSC mini-modules comprising two active strips 0.8cm×5.0cm were fabricated.

Figure 6.1a shows the structure of each module. The TiO_2 photoanode in this case was sensitized with the indoline dye D102, which typically is found to give a power conversion efficiency of around 3.5% using the standard fabrication protocol (for example see [46]), with the hole transporter spiro-OMeTAD. Each active strip has the same area in order that they generate equal currents — when multiple cells are connected in series conservation of charge dictates that overall performance will be limited by the cell gener-

ating the least current. To prevent possible shorting paths arising between the TiO_2 and the evaporated silver cathodes, a 500nm layer of insulating mesoporous Al_2O_3 was added as a buffer layer on top of the standard TiO_2 anodes. [16]

To optimize the pore-filling fraction, attempts were made to alter the wettability and drying rate of the spiro-OMeTAD solution by heating the substrates prior to and during the doctor-blading process. Figure 6.2 shows the mini-module performance parameters extracted from current voltage measurements under simulated AM 1.5 100mWcm^{-2} solar illumination as a function of coating temperature.

A clear trend in performance with changing deposition temperature is observed. Power conversion efficiency and short-circuit current density both peak with values of 2.6% and 3.8mAcm^{-2} respectively when the substrate is coated at 70°C. All parameters get worse above this temperature. It is hypothesized that this trend is due to competition between increasing wettability of the spiro-OMeTAD solution, and increasing solvent evaporation rate. As the temperature is increased up to 70°C the decreasing solution viscosity aids the surface wetting of the TiO_2 and helps material flow into the pores. Beyond 70°C the increased solvent evaporation rate becomes the dominant factor inhibiting the amount of hole-transporter infiltrating the photoanode — possibly due to too large a concentration gradient being set up within the drying spiro-OMeTAD film, causing an early onset of skin formation. It is noted that the fill factor does not follow this trend: the variation can be attributed to several factors, for example the thickness of the spiro-OMeTAD capping layer (which typically varies between samples)

and the added complications of having multiple active areas — whilst every effort was made to make each sub-cell the same area, it is likely that there is some degree of current mismatch since all alignment in the etching and cell definition process was done by hand.

In order to investigate these hypotheses, pore-filling measurements using absorption spectroscopy were performed on similar substrates to those used in the devices (see experimental details, section 2.1). The method used is described in detail elsewhere, and the relevant calculations are summarised in chapter 1. [46] In brief, by looking at the frequency of Fresnel interference fringes in the transmission spectra using below band-gap radiation, a wavelength averaged effective refractive index, $n_{av,eff}$, as defined by Docampo et al. can be calculated (an example spectra is shown in figure 6.3a). [46] This is done before and after coating the mesoporous TiO_2 with spiro-OMeTAD, and employing an effective medium approximation allows the fractional composition of TiO_2, air and spiro-OMeTAD, and hence the pore-filling fraction to be determined. In order to obtain the most accurate data, the substrates used for the pore-filling measurements were coated on flat glass and had no dye adsorbed on the TiO_2. It has previously been verified that the presence of the dye has surprisingly little influence upon the pore filling of spiro-OMeTAD into the mesoporous TiO_2. [46] The substrates did not include the additional layer of mesoporous Al_2O_3 featured in the modules to avoid complicating the interference patterns.

The results are shown in figure 6.3. The same trend in pore-filling with respect to temperature is seen as with the mini-module performance parameters, with filling fraction peaking at 70°C. This supports the hypothesis that

changes in pore-filling fraction are responsible for changes in device performance. Though the absolute values are an estimate only (as the samples used for pore filling measurements are a simplified version of the modules themselves), the relationship between PFF and PCE also match data reported by Docampo et al. for small area spin-cast devices very well. The maximum pore-filling fraction of 41% estimated here is still less than the minimum 60% required for maximum device performance, though it is close to the threshold. [46] It is likely that this sub-optimal pore filling is largely responsible for the difference in efficiency between these mini-modules and standard small test devices, fabricated with optimum pore-filling. Indeed it is expected that a small lab scale device employing D102 as the sensitizer with around 40% pore filling to only have around 2.5% PCE. [46] Hence, further optimisation of the doctor-blade coating conditions, i.e. solvent, temperature and coating rate, or moving to other more suitable large area deposition techniques are likely to give very small losses in the scale-up of solid-state DSSCs.

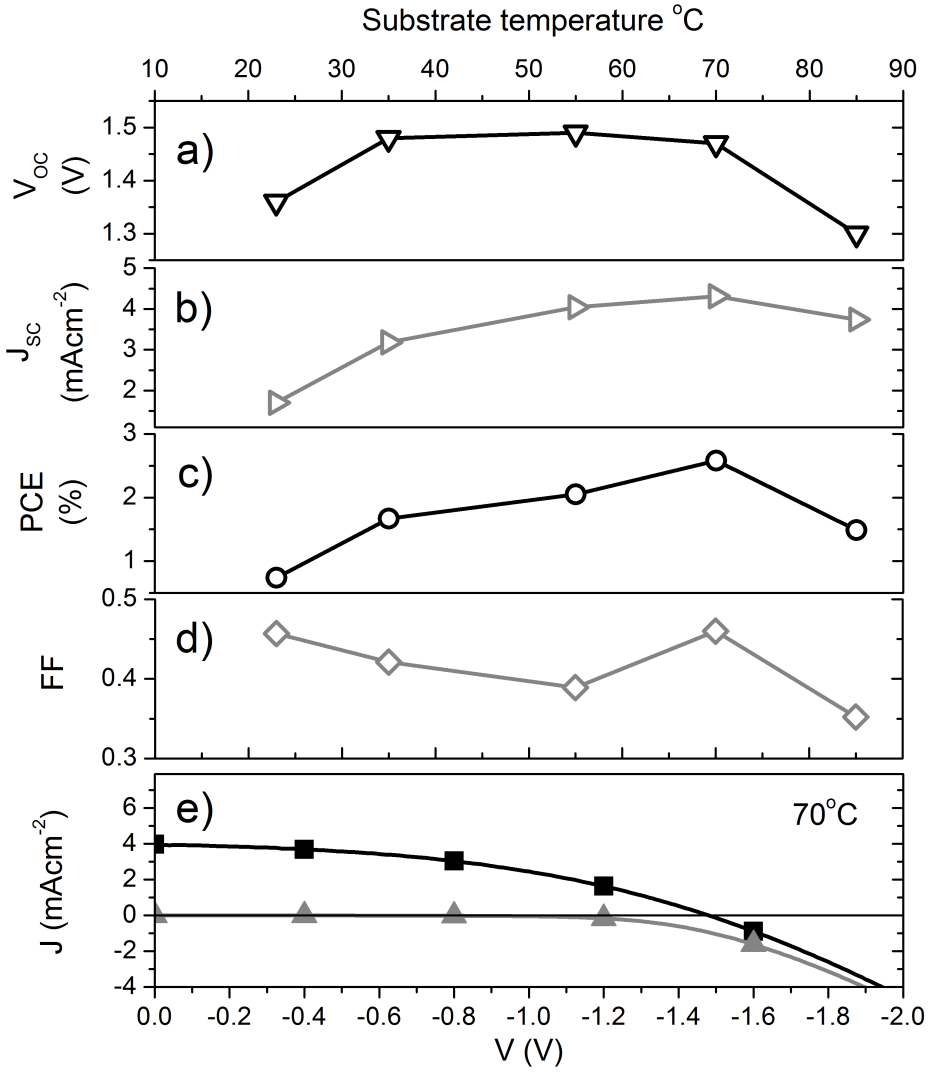

Figure 6.2: Solar cell performance parameters for 8cm^2 two-cell mini-modules as a function of substrate temperature during doctor blade deposition of spiro-OMeTAD, measured under simulated AM 1.5 100mWcm^{-2} illumination at room temperature: a) open-circuit voltage (V_{OC}); b) short-circuit current density (J_{SC}); c) power conversion efficiency (PCE); d) fill factor (FF); e) Current-voltage curves for the best performing mini-module under illumination (black squares) and in the dark (grey triangles). It is noted that the active area of the mini-modules was defined by the overlap of the metal electrodes and FTO, and not by a non-transparent optical mask as would be the ideal method. Edge effects are likely to introduce a slight overestimation in the photocurrent, though considerably less in this large cell configuration than the 14% increase reported for small area (0.12cm^2) solid-state DSSCs, but should still be considered when comparing absolute values. [40]

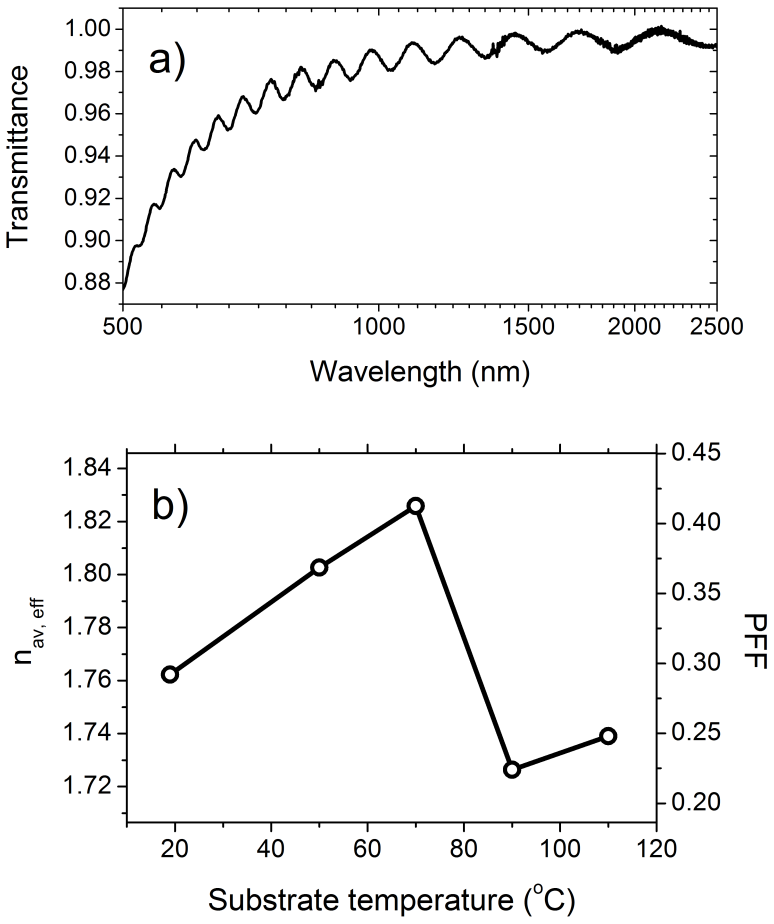

Figure 6.3: a) Example transmission spectra for a sample of TiO_2 before coating with spiro-OMeTAD showing Fresnel interference fringes. b) Average effective refractive index ($n_{av,eff}$, as defined by Docampo et al. [46] and volume fraction of mesoporous TiO_2 infiltrated by spiro-OMeTAD (pore-filling fraction, PFF) as a function of substrate temperature during deposition.

6.3 Conclusion

It has been successfully demonstrated that mini-modular fabrication of solid-state dye-sensitized solar cells is possible, and has been shown that using the simple and scalable technique of hole-transporter doctor-blading it is possible to achieve efficiencies approaching those of the small area test devices typically constructed for research. By varying the substrate temperature during deposition the extent to which the hole-transporter infiltrates the pores can be tuned to achieve best performance. In the case of spiro-OMeTAD it was found that the maximum pore-filling fraction to be 41% at a substrate deposition temperature of 70°C. If this can be increased to above 60% through optimised coating or more suitable choice of solvents, it is reasonable to expect negligible losses when going from the less than 1cm^2 laboratory-scale devices to large area modules.

Chapter 7

Conclusions

This thesis has focussed on the dual themes of enhancing the power conversion efficiency of solid-state dye sensitized solar cell technology through better electronic contact and increasing harvesting of solar radiation in single devices using a hybrid tandem architecture, and on assuring the suitability of DSSCs for large scale fabrication.

Chapters 3 and 4 describe two very different routes to improving DSSC performance though modification of the hole transporter/cathode interface. The altered energy band profile upon the addition of tungsten or molybdenum disulphide layers to films of spiro-OMeTAD appears to facilitate better hole extraction, observed in increased currents and power conversion efficiencies in solar cell devices. This work shows not only the effectiveness of these materials, but also that they may be processed from solution in a manner that is compatible with scalable production methods. Similarly, the addition of a heavily *p*-type doped spiro-OMeTAD nanoparticle layer between the bulk hole transporter and silver electrodes showed improved device performance.

The novelty of this structure lies in the use of the mini-emulsion processing technique to make a dispersion of doped hole transporter nanoparticles in an orthogonal solvent. This is one solution to a recurring issue in organic electronics, namely how to process multiple components on top of one another without damaging the layer underneath if they are soluble in the same casting solvents. However for both the TMDC and doped organic nanoparticle interlayers, SEM imaging has shown present deposition methods are far from optimal, with large areas of bulk hole transporter film left uncovered by the interface modification materials. Given the positive results seen in the device performance characteristics, it is perfectly possible that optimisation of the coating processing method for each material could yield even more efficient solar cells.

Despite the success in demonstrating the effectiveness of novel hole extraction layers, attempts to incorporate them into series recombination interconnects in tandem solar cells were ultimately unsuccessful. Solid-state DSSC sub-cells using a dye sensitive towards the higher energy end of the solar spectrum and bulk heterojunction sub-cells using a low band gap polymer sensitive out into the infra-red were tested in isolation to confirm their suitability for use together in a tandem device. Unfortunately all recombination interconnects tested, including those previously described in literature fell short of targets to increase open circuit voltage beyond that of either sub-cell in isolation. This is most probably due to imperfect film morphology, and it remains to be seen whether tandem devices incorporating DSSCs with flat spiro-OMeTAD capping layers will function more effectively.

To ensure the viability of solid-state DSSC systems as commercial tech-

nologies, the ability to fabricate functioning devices on large areas is critically important. With this in mind, hole transporter deposition over large areas was successfully demonstrated using doctor blade coating, as opposed to spin coating as used on small test cells. To do this, two strip mini-modules were made with silver interconnects and a total 8cm^2 active area. By tuning the pore filling fraction by altering the substrate temperature during deposition, a respectable peak efficiency of 2.6% was obtained with the dye D102, only about 25% less than the efficiency typically obtained in small area test devices.

7.1 Potential future work

There are a number of logical extensions to, and progressions from the work described here that could be followed up in future. An obvious one that could yield significant improvement is the optimisation of the hole extraction interface deposition mentioned in chapters 3 and 4. In the first instance for TMDCs it may be useful to use the same method of coating as previously described, but use an ultrasonic spray nozzle which could perhaps distribute material more evenly across the devices. Aerosol deposition may also prove to have an advantage over spin coating in the case of the *p*-spiro-OMeTAD nanoparticle dispersion. Another option would be to vary the surface wettability, for instance by changing the dispersion solvent, through the use of chemical surfactants, or by subjecting the DSSC to oxygen plasma before coating the hole extraction layer — a technique commonly used to chemically activate the surfaces of organic materials to improve wettability. [92,93] Care

would need to be taken in the latter case however, as experience has shown that plasma treatment can also easily damage the organic components.

The goal of achieving effective tandem solar cells incorporating a solid-state DSSC sub-cell has not been realised. Further development of the series interconnect components and particularly sourcing hole transporter material that is not susceptible to intermittent issues with de-wetting and droplet formation should go a long way to fabricating such a device. Future work does not need to be limited to using polymer bulk heterojunction sub-cells — an exciting alternative would be to incorporate the recently discovered organometal halide perovskite solar cell, used with a solid-state DSSC with complementary absorption. [94, 95]

There is scope for further work on large area hole transporter deposition as well. It may be possible to further improve pore filling fractions though the use of different HTM solution concentrations or different carrier solvents to achieve an optimal viscosity. In addition, it would be useful to scale up devices to yet larger modules, with longer active strips and more of them to reinforce confidence in solid state DSSC scalability. It should also be noted that hole transporter coating is not the last step in making fully commercial solid state DSSCs — in all experiments carried out in this work evaporation under vacuum was required for silver electrode deposition. This is more expensive to scale up than solution processing techniques and is at odds with the often stressed desire for cheap, vacuum-free manufacture techniques. Though beyond the scope of the work presented in this thesis, it is arguably of significant importance to design contacts to external circuitry that are in some way compatible with reel-to-reel or solution-based processes for solid-

state DSSCs to be truly successful.

Appendix

Publications

1. P. Docampo, **A. Hey**, S. Guldin, R. Gunning, U. Steiner, H. J. Snaith, "Pore Filling of Spiro-OMeTAD in Solid-State Dye-Sensitized Solar Cells Determined Via Optical Reflectometry," *Advanced Functional Materials*, vol. 22, no. 23, pp. 5010-5019, 2012.

2. J. M. Ball, M. M. Lee, **A. Hey**, H. Snaith, "Low-Temperature Processed Mesosuperstructured to Thin-Film Perovskite Solar Cells," *Energy & Environmental Science*, vol. 6, pp. 1739-1743, 2013.

3. **A. Hey**, H. J. Snaith, "Large Area Hole Transporter Deposition in Efficient Solid-state Dye-sensitized Solar Cell Mini-modules," *Journal of Applied Physics*, accepted.

4. **A. Hey**, V. Nicolosi, H. J. Snaith, "Transition Metal Dichalcogenide Hole Extraction Layers for Dye-sensitized Solar cells," in preparation.

International conference poster presentations

1. **A. Hey**, H. J. Snaith, "Hole Transporter Coating of Large Area Solid-State Dye-Sensitized Solar Cells," HOPV meeting in Valencia, May 2011.

2. **A. Hey**, H. J. Snaith, "Hole Transporter Coating of Large Area Solid-State Dye-Sensitized Solar Cells," JUDO-PV meeting in Oxford, July 2011.

Bibliography

[1] J. Dempsey, "Merkel loses key german state on nuclear fears," *New York Times, http://www.nytimes.com/2011/03/28/world/europe/28germany.html*, Accessed 11 March 2013.

[2] P. Moriarty and D. Honnery, "What is the global potential for renewable energy?," *Renewable and Sustainable Energy Reviews*, vol. 16, no. 1, pp. 244–252, 2012.

[3] I. E. Agency, "Topic: Solar (pv and csp)," *http://www.iea.org/topics/solarpvandcsp/*, Accessed 17 Jan 2013.

[4] U. E. I. Administration, "Levelized cost of new generation resources in the annual energy outlook 2012," *http://www.eia.gov/forecasts/aeo/electricity_generation.cfm*, Accessed 17 Jan 2013.

[5] D. M. Chapin, C. S. Fuller, and G. L. Pearson, "A new silicon p-n junction photocell for converting solar radiation into electrical power," *Journal of Applied Physics*, vol. 25, no. 5, pp. 676–677, 1954.

[6] M. A. Green, K. Emery, Y. Hishikawa, W. Warta, and E. D. Dunlop, "Solar cell efficiency tables (version 41)," *Progress in Photovoltaics: Research and Applications*, vol. 21, no. 1, pp. 1–11, 2013.

[7] H. M. Rosenberg, *The Solid State*. Oxford Physics Series, Oxford University Press, 2 ed., 1978.

[8] J. Nelson, *The Physics of Solar Cells*. Imperial College Press, 2004.

[9] G. A. Chamberlain, "Organic solar cells: A review," *Solar Cells*, vol. 8, no. 1, pp. 47–83, 1983.

[10] C. Kittel, *Introduction to Solid State Physics*. Wiley, 5 ed., 1953.

[11] J. Moser, "Notiz über verstärkung photoelektrischer ströme durch optische sensibilisirung," *Monatshefte für Chemie und verwandte Teile anderer Wissenschaften*, vol. 8, no. 1, pp. 373–373, 1887.

[12] B. O'Regan and M. Grätzel, "A low-cost, high-efficiency solar cell based on dye-sensitized colloidal tio2 films," *Nature*, vol. 353, no. 6346, pp. 737–740, 1991. 10.1038/353737a0.

[13] B. E. Hardin, H. J. Snaith, and M. D. McGehee, "The renaissance of dye-sensitized solar cells," *Nat Photon*, vol. 6, no. 3, pp. 162–169, 2012. 10.1038/nphoton.2012.22.

[14] H. J. Snaith and L. Schmidt-Mende, "Advances in liquid-electrolyte and solid-state dye-sensitized solar cells," *Advanced Materials*, vol. 19, no. 20, pp. 3187–3200, 2007.

[15] N. A. Anderson and T. Lian, "Ultrafast electron injection from metal polypyridyl complexes to metal-oxide nanocrystalline thin films," *Coordination Chemistry Reviews*, vol. 248, no. 1314, pp. 1231–1246, 2004.

[16] P. Docampo and H. J. Snaith, "Obviating the requirement for oxygen in sno2-based solid-state dye-sensitized solar cells," *Nanotechnology*, vol. 22, no. 22, 2011.

[17] M. Quintana, T. Edvinsson, A. Hagfeldt, and G. Boschloo, "Comparison of dye-sensitized zno and tio2 solar cells: studies of charge transport and carrier lifetime," *The Journal of Physical Chemistry C*, vol. 111, no. 2, pp. 1035–1041, 2006.

[18] B. Liu and E. S. Aydil, "Growth of oriented single-crystalline rutile tio2 nanorods on transparent conducting substrates for dye-sensitized solar cells," *Journal of the American Chemical Society*, vol. 131, no. 11, pp. 3985–3990, 2009.

[19] G. K. Mor, K. Shankar, M. Paulose, O. K. Varghese, and C. A. Grimes, "Use of highly-ordered tio2 nanotube arrays in dye-sensitized solar cells," *Nano Letters*, vol. 6, no. 2, pp. 215–218, 2005.

[20] S. Guldin, P. Docampo, M. Stefik, G. Kamita, U. Wiesner, H. J. Snaith, and U. Steiner, "Layer-by-layer formation of block-copolymer-derived tio2 for solid-state dye-sensitized solar cells," *Small*, vol. 8, no. 3, pp. 432–440, 2012.

[21] J. Nelson, "Continuous-time random-walk model of electron transport in nanocrystalline tio$_2$ electrodes," *Physical Review B*, vol. 59, no. 23, pp. 15374–15380, 1999.

[22] T. Tiedje and A. Rose, "A physical interpretation of dispersive transport in disordered semiconductors," *Solid State Communications*, vol. 37, no. 1, pp. 49–52, 1981.

[23] G. Boschloo and A. Hagfeldt, "Characteristics of the iodide/triiodide redox mediator in dye-sensitized solar cells," *Acc. Chem. Res.*, vol. 42, no. 11, pp. 1819–1826, 2009.

[24] M. Grätzel, "Recent advances in sensitized mesoscopic solar cells," *Accounts of Chemical Research*, vol. 42, no. 11, pp. 1788–1798, 2009.

[25] E. Olsen, G. Hagen, and S. Eric Lindquist, "Dissolution of platinum in methoxy propionitrile containing lii/i2," *Solar Energy Materials and Solar Cells*, vol. 63, no. 3, pp. 267–273, 2000.

[26] U. Bach, D. Lupo, P. Comte, J. E. Moser, F. Weissortel, J. Salbeck, H. Spreitzer, and M. Grätzel, "Solid-state dye-sensitized mesoporous tio2 solar cells with high photon-to-electron conversion efficiencies," *Nature*, vol. 395, no. 6702, pp. 583–585, 1998. 10.1038/26936.

[27] D. Poplavskyy and J. Nelson, "Nondispersive hole transport in amorphous films of methoxy-spirofluorene-arylamine organic compound," *Journal of Applied Physics*, vol. 93, no. 1, pp. 341–346, 2003.

[28] J. Burschka, A. Dualeh, F. Kessler, E. Baranoff, N. L. Cevey-Ha, C. Yi, M. K. Nazeeruddin, and M. Grätzel, "Tris(2-(1h-pyrazol-1-yl)pyridine)cobalt(iii) as p-type dopant for organic semiconductors and its application in highly efficient solid-state dye-sensitized solar cells," *J. Am. Chem. Soc.*, vol. 133, no. 45, pp. 18042–5, 2011.

[29] N. R. R. D. Centre, "Reference solar spectral irradiance: Air mass 1.5," *http://rredc.nrel.gov/solar/spectra/am1.5/*, Accessed 03 Feb 2013.

[30] A. Hadipour, B. deBoer, and P. W. M. Blom, "Organic tandem and multi-junction solar cells," *Advanced Functional Materials*, vol. 18, no. 2, pp. 169–181, 2008.

[31] I. Bruder, M. Karlsson, F. Eickemeyer, J. Hwang, P. Erk, A. Hagfeldt, J. Weis, and N. Pschirer, "Efficient organic tandem cell combining a solid state dye-sensitized and a vacuum deposited bulk heterojunction solar

cell," *Solar Energy Materials and Solar Cells*, vol. 93, no. 10, pp. 1896–1899, 2009.

[32] C. W. Tang, "Two-layer organic photovoltaic cell," *Applied Physics Letters*, vol. 48, no. 2, pp. 183–185, 1986.

[33] P. W. M. Blom, V. D. Mihailetchi, L. J. A. Koster, and D. E. Markov, "Device physics of polymer:fullerene bulk heterojunction solar cells," *Advanced Materials*, vol. 19, no. 12, pp. 1551–1566, 2007.

[34] P. E. Shaw, A. Ruseckas, and I. D. W. Samuel, "Exciton diffusion measurements in poly(3-hexylthiophene)," *Advanced Materials*, vol. 20, no. 18, pp. 3516–3520, 2008.

[35] W.-H. Baek, M. Choi, T.-S. Yoon, H. H. Lee, and Y.-S. Kim, "Use of fluorine-doped tin oxide instead of indium tin oxide in highly efficient air-fabricated inverted polymer solar cells," *Applied Physics Letters*, vol. 96, no. 13, pp. 133506–3, 2010.

[36] L. Schmidt-Mende, U. Bach, R. Humphry-Baker, T. Horiuchi, H. Miura, S. Ito, S. Uchida, and M. Grätzel, "Organic dye for highly efficient solid-state dye-sensitized solar cells," *Advanced Materials*, vol. 17, no. 7, pp. 813–815, 2005.

[37] H. J. Snaith and M. Gräzel, "Enhanced charge mobility in a molecular hole transporter via addition of redox inactive ionic dopant: Implication to dye-sensitized solar cells," *Appl. Phys. Lett.*, vol. 89, no. 26, p. 262114, 2006.

[38] T. M. Clarke, A. M. Ballantyne, J. Nelson, D. D. C. Bradley, and J. R. Durrant, "Free energy control of charge photogeneration in polythiophene/fullerene solar cells: The influence of thermal annealing on p3ht/pcbm blends," *Adv. Funct. Mater.*, vol. 18, no. 24, pp. 4029–4035, 2008.

[39] J. Peet, J. Y. Kim, N. E. Coates, W. L. Ma, D. Moses, A. J. Heeger, and G. C. Bazan, "Efficiency enhancement in low-bandgap polymer solar cells by processing with alkane dithiols," *Nat Mater*, vol. 6, no. 7, pp. 497–500, 2007. 10.1038/nmat1928.

[40] H. J. Snaith, "How should you measure your excitonic solar cells?," *Energy & Environmental Science*, vol. 5, no. 4, pp. 6513–6520, 2012.

[41] S. A. Gevorgyan, J. Eggert Carlé, R. Søndergaard, T. Trofod Larsen-Olsen, M. Jørgensen, and F. C. Krebs, "Accurate characterization of opvs: Device masking and different solar simulators," *Solar Energy Materials and Solar Cells*, vol. 110, no. 0, pp. 24–35, 2013.

[42] H. J. Snaith, R. Humphry-Baker, P. Chen, I. Cesar, S. M. Zakeeruddin, and M. Grätzel, "Charge collection and pore filling in solid-state dye-sensitized solar cells," *Nanotechnology*, vol. 19, no. 42, p. 424003, 2008.

[43] I. K. Ding, N. Tétreault, J. Brillet, B. E. Hardin, E. H. Smith, S. J. Rosenthal, F. Sauvage, M. Grätzel, and M. D. McGehee, "Pore-filling of spiro-ometad in solid-state dye sensitized solar cells: Quantification, mechanism, and consequences for device performance," *Adv. Funct. Mater.*, vol. 19, no. 15, pp. 2431–2436, 2009.

[44] A. Abrusci, I. K. Ding, M. Al-Hashimi, T. Segal-Peretz, M. D. McGehee, M. Heeney, G. L. Frey, and H. J. Snaith, "Facile infiltration of semiconducting polymer into mesoporous electrodes for hybrid solar cells," *Energy & Environmental Science*, vol. 4, no. 8, p. 3051, 2011.

[45] J. Melas-Kyriazi, I. K. Ding, A. Marchioro, A. Punzi, B. E. Hardin, G. F. Burkhard, N. Tétreault, M. Grätzel, J.-E. Moser, and M. D. McGehee, "The effect of hole transport material pore filling on photovoltaic performance in solid-state dye-sensitized solar cells," *Advanced Energy Materials*, vol. 1, no. 3, pp. 407–414, 2011.

[46] P. Docampo, A. Hey, S. Guldin, R. Gunning, U. Steiner, and H. J. Snaith, "Pore filling of spiro-ometad in solid-state dye-sensitized solar cells determined via optical reflectometry," *Advanced Functional Materials*, vol. 22, no. 23, pp. 5010–5019, 2012.

[47] C. Pickering, M. I. J. Beale, D. J. Robbins, P. J. Pearson, and R. Greef, "Optical properties of porous silicon films," *Thin Solid Films*, vol. 125, no. 12, pp. 157–163, 1985.

[48] D. A. G. Bruggeman, "Berechnung verschiedener physikalischer konstanten von heterogenen substanzen. i. dielektrizitätskonstanten und leitfähigkeiten der mischkörper aus isotropen substanzen," *Annalen der Physik*, vol. 416, no. 7, pp. 636–664, 1935.

[49] E. Voroshazi, B. Verreet, A. Buri, R. Müller, D. Di Nuzzo, and P. Heremans, "Influence of cathode oxidation via the hole extraction layer in polymer:fullerene solar cells," *Organic Electronics*, vol. 12, no. 5, pp. 736–744, 2011.

[50] M. Jørgensen, K. Norrman, and F. C. Krebs, "Stability/degradation of polymer solar cells," *Solar Energy Materials and Solar Cells*, vol. 92, no. 7, pp. 686–714, 2008.

[51] H. Yan, P. Lee, N. R. Armstrong, A. Graham, G. A. Evmenenko, P. Dutta, and T. J. Marks, "High-performance hole-transport layers for polymer light-emitting diodes. implementation of organosiloxane cross-linking chemistry in polymeric electroluminescent devices," *Journal of the American Chemical Society*, vol. 127, no. 9, pp. 3172–3183, 2005.

[52] T. Stubhan, N. Li, N. A. Luechinger, S. C. Halim, G. J. Matt, and C. J. Brabec, "High fill factor polymer solar cells incorporating a low temperature solution processed wo3 hole extraction layer," *Advanced Energy Materials*, pp. 1433–1438, 2012.

[53] V. Shrotriya, G. Li, Y. Yao, C.-W. Chu, and Y. Yang, "Transition metal oxides as the buffer layer for polymer photovoltaic cells," *Applied Physics Letters*, vol. 88, no. 7, pp. 073508–3, 2006.

[54] Q. H. Wang, K. Kalantar-Zadeh, A. Kis, J. N. Coleman, and M. S. Strano, "Electronics and optoelectronics of two-dimensional transition metal dichalcogenides," *Nat Nano*, vol. 7, no. 11, pp. 699–712, 2012. 10.1038/nnano.2012.193.

[55] J. A. Wilson and A. D. Yoffe, "The transition metal dichalcogenides discussion and interpretation of the observed optical, electrical and structural properties," *Advances in Physics*, vol. 18, no. 73, pp. 193–335, 1969.

[56] G. L. Frey, K. J. Reynolds, and R. H. Friend, "Novel electrodes from solution-processed layer-structure materials," *Advanced Materials*, vol. 14, no. 4, pp. 265–268, 2002.

[57] K. J. Reynolds, J. A. Barker, N. C. Greenham, R. H. Friend, and G. L. Frey, "Inorganic solution-processed hole-injecting and electron-blocking layers in polymer light-emitting diodes," *J. Appl. Phys.*, vol. 92, no. 12, p. 7556, 2002.

[58] G. L. Frey, K. J. Reynolds, R. H. Friend, H. Cohen, and Y. Feldman, "Solution-processed anodes from layer-structure materials for high-efficiency polymer light-emitting diodes," *Journal of the American Chemical Society*, vol. 125, no. 19, pp. 5998–6007, 2003.

[59] S. J. Li, Z. Chen, and W. F. Zhang, "Dye-sensitized solar cells based on ws2 counter electrodes," *Mater. Lett.*, vol. 72, pp. 22–24, 2012.

[60] M. Kröger, S. Hamwi, J. Meyer, T. Riedl, W. Kowalsky, and A. Kahn, "P-type doping of organic wide band gap materials by transition metal oxides: A case-study on molybdenum trioxide," *Organic Electronics*, vol. 10, no. 5, pp. 932–938, 2009.

[61] T. Leijtens, I. K. Ding, T. Giovenzana, J. T. Bloking, M. D. McGehee, and A. Sellinger, "Hole transport materials with low glass transition temperatures and high solubility for application in solid-state dye-sensitized solar cells," *ACS Nano*, vol. 6, no. 2, pp. 1455–1462, 2012.

[62] Y. Xu and M. A. A. Schoonen, "The aboslute energy positions of conduction and valance bands of selected semiconducting minerals," *Am. Mineral.*, vol. 85, pp. 543–556, 2000.

[63] J. N. Coleman, M. Lotya, A. ONeill, S. D. Bergin, P. J. King, U. Khan, K. Young, A. Gaucher, S. De, R. J. Smith, I. V. Shvets, S. K. Arora, G. Stanton, H.-Y. Kim, K. Lee, G. T. Kim, G. S. Duesberg, T. Hallam, J. J. Boland, J. J. Wang, J. F. Donegan, J. C. Grunlan, G. Moriarty, A. Shmeliov, R. J. Nicholls, J. M. Perkins, E. M. Grieveson, K. Theuwissen, D. W. McComb, P. D. Nellist, and V. Nicolosi, "Two-dimensional nanosheets produced by liquid exfoliation of layered materials," *Science*, vol. 331, no. 6017, pp. 568–571, 2011.

[64] K. Landfester, R. Montenegro, U. Scherf, R. Güntner, U. Asawapirom, S. Patil, D. Neher, and T. Kietzke, "Semiconducting polymer nanospheres in aqueous dispersion prepared by a miniemulsion process," *Advanced Materials*, vol. 14, no. 9, pp. 651–655, 2002.

[65] P. Wei, J. H. Oh, G. Dong, and Z. Bao, "Use of a 1h-benzoimidazole derivative as an n-type dopant and to enable air-stable solution-processed n-channel organic thin-film transistors," *Journal of the American Chemical Society*, vol. 132, no. 26, pp. 8852–8853, 2010.

[66] W. Geens, T. Martens, J. Poortmans, T. Aernouts, J. Manca, L. Lutsen, P. Heremans, S. Borghs, R. Mertens, and D. Vanderzande, "Modelling the short-circuit current of polymer bulk heterojunction solar cells," *Thin Solid Films*, vol. 451452, no. 0, pp. 498–502, 2004.

[67] P. Wei, T. Menke, B. D. Naab, K. Leo, M. Riede, and Z. Bao, "2-(2-methoxyphenyl)-1,3-dimethyl-1h-benzoimidazol-3-ium iodide as a new

air-stable n-type dopant for vacuum-processed organic semiconductor thin films," *Journal of the American Chemical Society*, vol. 134, no. 9, pp. 3999–4002, 2012.

[68] H. J. Snaith and R. H. Friend, "Photovoltaic devices fabricated from an aqueous dispersion of polyfluorene nanoparticles using an electroplating method," *Synthetic Metals*, vol. 147, no. 13, pp. 105–109, 2004.

[69] S. Yoo, J. Kum, and S. Cho, "Tuning the electronic band structure of pcbm by electron irradiation," *Nanoscale Research Letters*, vol. 6, no. 1, p. 545, 2011.

[70] A. Welte, C. Waldauf, C. Brabec, and P. J. Wellmann, "Application of optical absorbance for the investigation of electronic and structural properties of solgel processed tio2 films," *Thin Solid Films*, vol. 516, no. 20, pp. 7256–7259, 2008.

[71] A. Nattestad, A. J. Mozer, M. K. R. Fischer, Y. B. Cheng, A. Mishra, P. Bauerle, and U. Bach, "Highly efficient photocathodes for dye-sensitized tandem solar cells," *Nat Mater*, vol. 9, no. 1, pp. 31–35, 2010. 10.1038/nmat2588.

[72] M. Murayama and T. Mori, "Dye-sensitized solar cell using novel tandem cell structure," *Journal of Physics D: Applied Physics*, vol. 40, no. 6, p. 1664, 2007.

[73] D. Mühlbacher, M. Scharber, M. Morana, Z. Zhu, D. Waller, R. Gaudiana, and C. Brabec, "High photovoltaic performance of a low-bandgap polymer," *Advanced Materials*, vol. 18, no. 21, pp. 2884–2889, 2006.

[74] J. Gilot, M. M. Wienk, and R. A. J. Janssen, "Double and triple junction polymer solar cells processed from solution," *Appl. Phys. Lett.*, vol. 90, no. 14, p. 143512, 2007.

[75] S. K. Hau, H.-L. Yip, N. S. Baek, J. Zou, K. O'Malley, and A. K. Y. Jen, "Air-stable inverted flexible polymer solar cells using zinc oxide nanoparticles as an electron selective layer," *Applied Physics Letters*, vol. 92, no. 25, pp. 253301–3, 2008.

[76] S. Tanaka, K. Mielczarek, R. Ovalle-Robles, B. Wang, D. Hsu, and A. A. Zakhidov, "Monolithic parallel tandem organic photovoltaic cell with transparent carbon nanotube interlayer," *Appl. Phys. Lett.*, vol. 94, no. 11, p. 113506, 2009.

[77] Y. Zhou, C. Fuentes-Hernandez, J. W. Shim, T. M. Khan, and B. Kippelen, "High performance polymeric charge recombination layer for organic tandem solar cells," *Energy & Environmental Science*, 2012.

[78] S. Sista, M. H. Park, Z. Hong, Y. Wu, J. Hou, W. L. Kwan, G. Li, and Y. Yang, "Highly efficient tandem polymer photovoltaic cells," *Adv Mater*, vol. 22, no. 3, pp. 380–3, 2010. Sista, Srinivas Park, Mi-Hyae Hong, Ziruo Wu, Yue Hou, Jianhui Kwan, Wei Lek Li, Gang Yang, Yang Deerfield Beach, Fla. Adv Mater. 2010 Jan 19;22(3):380-3.

[79] T. Takamoto, E. Ikeda, H. Kurita, and M. Ohmori, "Over 30ingap/gaas tandem solar cells," *Applied Physics Letters*, vol. 70, no. 3, pp. 381–383, 1997.

[80] B. P. Rand, P. Peumans, and S. R. Forrest, "Long-range absorption enhancement in organic tandem thin-film solar cells containing silver nanoclusters," *Journal of Applied Physics*, vol. 96, no. 12, pp. 7519–7526, 2004.

[81] A. Hadipour, B. de Boer, and P. W. M. Blom, "Device operation of organic tandem solar cells," *Organic Electronics*, vol. 9, no. 5, pp. 617–624, 2008.

[82] J. M. Ball, M. M. Lee, A. Hey, and H. Snaith, "Low-temperature processed mesosuperstructured to thin-film perovskite solar cells," *Energy & Environmental Science*, 2013.

[83] F. Liu and J.-M. Nunzi, "Air stable hybrid inverted tandem solar cell design," *Applied Physics Letters*, vol. 99, no. 6, pp. 063301–3, 2011.

[84] J. Y. Kim, K. Lee, N. E. Coates, D. Moses, T. Q. Nguyen, M. Dante, and A. J. Heeger, "Efficient tandem polymer solar cells fabricated by all-solution processing," *Science*, vol. 317, no. 5835, pp. 222–5, 2007. Kim, Jin Young Lee, Kwanghee Coates, Nelson E Moses, Daniel Nguyen, Thuc-Quyen Dante, Mark Heeger, Alan J New York, N.Y. Science. 2007 Jul 13;317(5835):222-5.

[85] F. C. Krebs, "Fabrication and processing of polymer solar cells: A review of printing and coating techniques," *Solar Energy Materials and Solar Cells*, vol. 93, no. 4, pp. 394–412, 2009.

[86] F. C. Krebs, "Polymer solar cell modules prepared using roll-to-roll methods: Knife-over-edge coating, slot-die coating and screen printing," *Solar Energy Materials and Solar Cells*, vol. 93, no. 4, pp. 465–475, 2009.

[87] L. Blankenburg, K. Schultheis, H. Schache, S. Sensfuss, and M. Schrödner, "Reel-to-reel wet coating as an efficient up-scaling technique for the production of bulk-heterojunction polymer solar cells," *Solar Energy Materials and Solar Cells*, vol. 93, no. 4, pp. 476–483, 2009.

[88] M. A. Green, K. Emery, Y. Hishikawa, W. Warta, and E. D. Dunlop, "Solar cell efficiency tables (version 39)," *Progress in Photovoltaics: Research and Applications*, vol. 20, no. 1, pp. 12–20, 2012.

[89] I. K. Ding, J. Melas-Kyriazi, N.-L. Cevey-Ha, K. G. Chittibabu, S. M. Zakeeruddin, M. Grätzel, and M. D. McGehee, "Deposition of hole-transport materials in solid-state dye-sensitized solar cells by doctor-blading," *Organic Electronics*, vol. 11, no. 7, pp. 1217–1222, 2010.

[90] A. Kay and M. Grätzel, "Low cost photovoltaic modules based on dye sensitized nanocrystalline titanium dioxide and carbon powder," *Solar Energy Materials and Solar Cells*, vol. 44, no. 1, pp. 99–117, 1996.

[91] J. J. Hanak, "Monolithic solar cell panel of amorphous silicon," *Solar Energy*, vol. 23, no. 2, pp. 145–147, 1979.

[92] H. J. Hettlich, F. Otterbach, C. Mittermayer, R. Kaufmann, and D. Klee, "Plasma-induced surface modifications on silicone intraocular lenses: chemical analysis and in vitro characterization," *Biomaterials*, vol. 12, no. 5, pp. 521–524, 1991.

[93] S. Bhattacharya, A. Datta, J. M. Berg, and S. Gangopadhyay, "Studies on surface wettability of poly(dimethyl) siloxane (pdms) and glass under oxygen-plasma treatment and correlation with bond strength," *Journal of Microelectromechanical Systems*, vol. 14, no. 3, pp. 590–597, 2005.

[94] M. M. Lee, J. Teuscher, T. Miyasaka, T. N. Murakami, and H. J. Snaith, "Efficient hybrid solar cells based on meso-superstructured organometal halide perovskites," *Science*, vol. 338, no. 6107, pp. 643–647, 2012.

[95] A. Kojima, K. Teshima, Y. Shirai, and T. Miyasaka, "Organometal halide perovskites as visible-light sensitizers for photovoltaic cells," *Journal of the American Chemical Society*, vol. 131, no. 17, pp. 6050–6051, 2009.